

EXTREME VACUUM TECHNOLOGY INCLUDING CRYOSORPTION,  
DIFFUSION PUMP AND PRESSURE CALIBRATION STUDIES

**N66 23795**

FACILITY FORM 802	(ACCESSION NUMBER)	(THRU)
	512	
	(PAGES)	(CODE)
	CR 74224	15
	(NASA CR OR TMX OR AD NUMBER)	(CATEGORY)

SUMMARY TECHNICAL REPORT

1 February 1965 - 1 March 1966

Contract NASr-63(06)

MRI Project No. 2675-P

GPO PRICE \$ \_\_\_\_\_  
CFSTI PRICE(S) \$ \_\_\_\_\_  
Hard copy (HC) \$ 3.00  
Microfiche (MF) 1.50

#653 July 65

For

Headquarters  
National Aeronautics and Space Administration  
Attn: Code SC  
Washington, D. C. 20546



MIDWEST RESEARCH INSTITUTE

425 VOLKER BOULEVARD/KANSAS CITY, MISSOURI 64110/AC 816 LO 1-0202

EXTREME VACUUM TECHNOLOGY INCLUDING CRYOSORPTION,  
DIFFUSION PUMP AND PRESSURE CALIBRATION STUDIES

by

Paul J. Bryant  
Charles M. Gosselin

SUMMARY TECHNICAL REPORT  
1 February 1965 - 1 March 1966

Contract NASr-63(06)

MRI Project No. 2675-P

For

Headquarters  
National Aeronautics and Space Administration  
Attn: Code SC  
Washington, D. C. 20546



MIDWEST RESEARCH INSTITUTE

425 VOLKER BOULEVARD/KANSAS CITY, MISSOURI 64110/AC 816 LO 1-0202

## PREFACE

The development of several phases of research relating to vacuum science and technology are included in this program. Mr. George Wise of the NASA Lewis Research Center is the technical monitor. This Summary Technical Report covers the period from 1 February 1965 to 1 March 1966.

The research activity is conducted in the Physics Department of the Midwest Research Institute under the direction of Dr. Sheldon L. Levy and Mr. Gordon E. Gross. Research activities were conducted by Dr. Paul Bryant, Mr. Charles Gosselin, Dr. William W. Longley and Mr. Lyle H. Taylor.

Approved for:

MIDWEST RESEARCH INSTITUTE



Sheldon L. Levy, Director  
Mathematics and Physics Division

31 March 1966

## TABLE OF CONTENTS

	<u>Page No.</u>
Summary . . . . .	1
I. Cryosorption Studies Including a Computer Program for Prediction of Cryopanel Operation . . . . .	2
A. Physical Adsorption Isotherm Theory . . . . .	2
B. Equipment Employed for Sensitive Adsorption Measurement . . . . .	5
C. Correlation of Adsorption Data with Theoretical Prediction . . . . .	8
II. Evaluation of a Dual Expansion Nozzle for Improved Diffusion Pump Operation . . . . .	20
A. Discussion of Diffusion Pump Operation . . . . .	20
B. Results and Conclusions . . . . .	23
III. Extreme Vacuum Measurement Techniques Including a Field Emission Microscope Study . . . . .	28
A. Cold Cathode Gauge Operation Based on a Magnetron Type Discharge . . . . .	28
B. Response Curves for Redhead, Kreisman, and Trigger Discharge Gauge Types . . . . .	32
C. A Field Emission Microscope Study . . . . .	37
IV. Dissemination of Information Dealing with Vacuum Science . .	44
References . . . . .	45
Appendix . . . . .	47

## TABLE OF CONTENTS (Continued)

### List of Figures

<u>Figure No.</u>	<u>Title</u>	<u>Page No.</u>
1	Adsorption Site Models for the Atomic Arrangement Used in the Development of the BET Theory (left and Triangular Site Model (right) . . . . .	12
2	Adsorption Geometry for the Triangular Model Showing: Nearest and Next Nearest Neighbor, and Interlayer Spacings; and First Adsorbed to Adsorbent Spacing, D . .	12
3	Microbalance System Attached to the PPAS . . . . .	13
4	Coaxial Vacuum Lead Assembly on Which Quartz Crystals are Mounted . . . . .	14
5	Lower End of Coaxial Vacuum Leads . . . . .	14
6	Schematic Diagram of a Stable 5 Mc. Oscillator . . . . .	15
7	Schematic Diagram of the Major Electronic and Environmental Components Used with the Microbalance System . . .	16
8	Experimental Data for Helium Adsorption on Aluminum Near 12°K; an Extremely High Sensitivity of about 200 Cycles/Monolayer is Indicated for the Piezoelectric Crystal Microbalance . . . . .	17
9	A Plot of the Surface Interaction Energy $W_s$ as a Function of Temperature According to Eq. (15) . . . . .	18
10	A Composite Plot of Experimental and Theoretical Adsorption Isotherms. . . . .	19
11	Schematic Diagram of a Dual Expansion Nozzle Assembly . . .	24
12	Schematic Diagram (right) and Photograph (left) of the Special Test Apparatus (modified) for Evaluation of Dual Expansion Diffusion Pump Nozzles . . . . .	25
13	Schematic Diagram (right) and Photograph (left) of the Vapor Jet Test System . . . . .	26
14	Graph of the Pumping Speed for a Single and Dual Expansion Nozzle as a Function of Boiler Temperature . . . . .	27
15	Graph of the Pressure Ratio Maintained Across the Jet Region for Both a Single and Dual Expansion Nozzle as a Function of Boiler Temperature. . . . .	27
16	Electron Orbits in a Coaxial Magnetron Structure. . . . .	38
17	Electrode Configurations of Commercial Magnetron Gauges, Shown to Scale in Cutaway; Anode Diameters: Redhead 3.0 cm., Kreisman 2.5 cm. . . . .	38

## TABLE OF CONTENTS (Concluded)

### List of Figures

<u>Figure No.</u>		<u>Page No.</u>
18	Characteristic Response of Clean Redhead (NRC 552 glass envelope) Gauges. . . . .	39
19	Characteristic Response of Clean Kreisman (GCA 1410) Gauges, Showing: Background Indicating $10^{-14}$ Torr Range For Pressure Below Threshold of $1.7 \times 10^{-10}$ Torr; a Rapid Buildup; a Possible Unstable Region Near $10^{-8}$ Torr; Followed By a Steady Sensitivity Rise Along a 1.11 Slope. . . . .	39
20	Characteristic Response Curves for Two Magnetron Gauge Models (upper portion of Redhead curve omitted) Showing Differences Which Result from Variations in the Designs .	40
21	An Example of Trigger Discharge Gauge, TDG, (GE Model 22 GT 214) Response Showing an Asymptotic Approach to a Residual Reading Which Distorts the Ion Current Response.	40
22	TDG Response for the UHV Range; the Ion Current Component Lies within the Shaded Region; Residual or Background Currents Can Give Higher Total Readings, e.g., see Circular Data Points; Loss of the Discharge and Ion Current May Give Lower Readings, e.g., see Triangular Data Points . . . . .	41
23	TDG Response above $10^{-8}$ Torr Giving Direct Readings from Gauge Control Unit with 2.5 Amp/Torr Sensitivity . . . .	42
24	Electron Field Emission Microscope Tube for Gas Dynamics Study; Metal Tip May Be Selectively Cooled without Significantly Cooling Inner Wall or Changing Equilibrium Gas Pressure . . . . .	43

## SUMMARY

23795

The research tasks of this program relate to the development and application of extreme vacuum science and technology. The tasks range from the production and calibration of extreme vacuum to a study of the cryosorption process.

A quartz piezoelectric crystal oscillator was designed and constructed for use as a microbalance.. The adsorption of helium gas on the crystal face at cryogenic temperatures near 12°K was measured. The oscillator and quartz resonator assembly has been operated successfully with a quarter of a microwatt of power through a pair of 33 in. coaxial leads. (This feat had to be accomplished to permit data collection within the UHV system cryopump.) The operational stability of the system and sensitivity permit the measurement of  $10^{-10}$  gm/cm<sup>2</sup>. A monolayer of helium weighs  $10^{-8}$  gm/cm<sup>2</sup>, so that monolayer adsorption of the light gas helium can be measured with 1 per cent accuracy.

Experimental data have been correlated via a new computer program with the theoretical isotherm developed earlier. Values were obtained for binding energy, interlayer spacing and other parameters relating to cryosorption. Both the computer program and the experimental equipment have been shown to be useful for predicting cryopanel operation.

Improved operation of a diffusion pump has been obtained by means of a dual expansion nozzle of the Flourescu type. The special jet design and the improvement of pumping speed are described.

A detailed study of the characteristics of cold cathode vacuum gauges has been conducted. Pressure response curves have been determined for the complete operating ranges of the commercial Redhead gauge (NRC Type 552), the Kreisman gauge (GCA Model 1410), and the GE Trigger Discharge gauge. A sensitive partial pressure analyzer has been used in conjunction with a field emission microscope to study gas dynamics at low pressures.

The information gained during the last year together with preceding results from Contract NASr-63(06) has been disseminated through a program of special seminars at each of the NASA branch laboratories. Consultation on special problems has been provided along with these visits to the various NASA facilities.

# I. CRYOSORPTION STUDIES INCLUDING A COMPUTER PROGRAM FOR PREDICTION OF CRYOPANEL OPERATION

The triangular site physical adsorption isotherm theory which has been developed on this program is correlated to experimental data. The study includes the development of a special piezoelectric crystal oscillation which is used as a sensitive microbalance. The experimental technique is presented in this section as well as a comparison between adsorption data and a theoretical approximation.

## A. Physical Adsorption Isotherm Theory

The physical adsorption isotherm theory developed earlier<sup>1,2/</sup> has been simplified by an approximation and compared with an experimental isotherm for helium adsorbed on an aluminum cryosurface at a representative temperature for cryopanel operation (about 12°K). The theoretical approximation uses the new triangular site model, as shown in Fig. 1, and includes the effects of the adsorbed particle interactions. For completeness, the theoretical isotherm equations will be specialized to the Lennard-Jones 6-12 intermolecular potential and closest packing of the adsorbed atoms (in previous notation this infers that  $R' = R$ ). Development of the isotherm is briefly summarized below.

Let the intermolecular potential between two adsorbed atoms be given by

$$\varphi(r) = 4\epsilon \left[ \left( \frac{\sigma}{r} \right)^{12} - \left( \frac{\sigma}{r} \right)^6 \right] \quad (1)$$

where  $r$  is the distance between the molecules,  $\epsilon$  is the maximum energy of attraction of the two atoms, and  $R = 2^{1/6}\sigma$  is the equilibrium distance between the atoms as shown in Fig. 2. All energies will actually be divided by the Boltzmann constant and expressed as degrees Kelvin. Equation (1) can be integrated over the various layers to give effective interaction energies which exclude the nearest neighbor interactions:

$$z(r) = 8\pi\epsilon\sigma_0 r^2 \left[ \frac{1}{4} \left( \frac{\sigma}{r} \right)^6 - \frac{1}{10} \left( \frac{\sigma}{r} \right)^{12} \right], \quad \sigma_0 = \frac{1.1547}{R^2} \quad (2)$$

where the values of  $r$  to be used (see Fig. 2) are given by

$$w = \left( \frac{\pi \sigma_o R^2}{4} \right)^{1/4} \sqrt{3} R ,$$

$$a = 0.81649 R , \quad a_j = (j-1)a ,$$

$$\rho = \left[ \frac{\pi \sigma_o (4R^2 + a^2)}{18} \right]^{1/4} \frac{4}{3} R^2 + a^2 . \quad (3)$$

The nearest neighbor interaction energy is simply  $\epsilon$  per pair interaction.

The interaction between an adsorbed atom and the adsorbent is treated as above with the energy for an atom in the first layer being given by

$$W_s = 10 \pi \epsilon_s N_o D^3/9 , \quad D = (0.4)^{1/6} r_s \quad (4)$$

where  $N$  is the number of adsorbent atoms per unit volume and  $\epsilon_s, \sigma_s$  are analogous to  $\epsilon, \sigma$ , respectively. For the  $j^{\text{th}}$  layer this energy becomes

$$W_{sj} = W_s \left[ \frac{9}{(1+d_j)^3} - \frac{3}{(1+d_j)^9} \right] , \quad d_j = a_j/D . \quad (5)$$

Using  $\theta_j$  for the fractional occupancy of the  $j^{\text{th}}$  layer, the effective adsorption energy can be written as

$$E_j = W_{sj} + 2P_{j-1}\epsilon + \frac{1}{2} (3+P_{j-1}\theta_{j-1}/\theta_j) F'_j \epsilon - \sum_{i=j+1}^J \frac{2^{i-j-1} \theta_i (P_{i-1} + P_i) \epsilon}{\theta_j}$$

$$+ 2C_j z(w) + 2(F'_j \theta_{j-1} + \theta_{j+1}) z(\rho) + 2 \sum_{i=1}^{j-2} \theta_i z(a_j - a_i) + 2 \sum_{i=j+2}^J \theta_i z(a_i - a_j) \quad (6)$$

where  $f'_j = 1 - \delta'_j$ ,  $P_j = \frac{\theta_{j+1}}{3\theta_j^3} P_{j-1}^2$ ,  $P_0 = 3C_1$  is a probability function for determining the likelihood of nearest neighbors and  $J$  is the number of the top layer.

Let

$$\gamma_j = (KM^{3/2} T^{5/2} / p) \exp(-E_j/T) \quad (7)$$

where  $K = 0.0256054$ ,  $M$  is the atomic mass of an adsorbed atom,  $T$  is the absolute temperature, and  $p$  is the gas pressure in Torr. The isotherm can then be calculated by iterating the  $J$  functions

$$\theta_j = \theta_{j-1}^3 \left[ 1 + \gamma_j \left( 1 - \theta_{j+1} \theta_j^{-3} \right)^{3\theta_j^2} \right]^{-1}, \quad \theta_0 = 1, \quad (8)$$

and summing over  $j$  to give the total number of adsorbed monolayers,  $\theta$ .

The above equations yield isotherms which exhibit discrete steps or are quite smooth.<sup>2/</sup> However, the equations are complicated and necessitate long computer times for their evaluation. An approximation which retains the essentials of the theory but needs only short computer times is the two-active layer approximation (the TAL theory). The TAL theory sets all  $N$  values of  $\theta_j$  greater than, say, 0.99 equal to 1 exactly and assumes that there are only two layers, the  $N+1$  and the  $N+2$  layers, which have  $\theta_j$  values between 0 and 1. The exact theory then reduces to a much simpler system. Let

$$V_{N+1} = W_{s,N+1} + \left[ 2 \sum_{i=1}^{N-1} z(a_j - a_i) + 3\epsilon + 2z(\rho) \right] f'_{N+1}, \quad (9)$$

$$U_{N+2} = W_{s,N+2} + 2 \sum_{i=1}^N z(a_j - a_i) + 3\epsilon,$$

then the TAL theory is given by Eq. (8) and

$$\theta = N + \theta_{N+1} + \theta_{N+2} ,$$

$$E_{N+1} = V_{N+1} + \left[ 2\theta_{N+1} - \left( \frac{\theta_{N+2}}{\theta_{N+1}} \right)^2 \right] 3\epsilon + 2\theta_{N+1}z(w) + 2\theta_{N+2}z(\rho) , \quad (10)$$

$$E_{N+2} = U_{N+2} + 6 \frac{\theta_{N+2}}{\theta_{N+1}} \epsilon + 2\theta_{N+1}z(\rho) + 2\theta_{N+2}z(w) .$$

This TAL theory still produces the discrete steps and smooth isotherms.

#### B. Equipment Employed for Sensitive Adsorption Measurement

A special piezoelectric crystal oscillator is used as a microbalance to measure the progressive loading of adsorbed layers as the pressure is gradually increased. The crystal's vibrational frequency, which decreases in proportion to the amount of adsorbed material, and the gas pressure have been accurately measured to form the experimental data.

The equipment needed to perform adsorption isotherm measurements is described here under two major categories: (1) environmental, and (2) electronic.

1. The environmental equipment requirements are determined by the following operational conditions: (a) The quartz crystal surfaces and its electrodes must be maintained in a noncontaminating atmosphere, viz., ultra-high vacuum; (b) the crystal must be maintained at a constant temperature, the level of which is established for the isotherm to be determined, and (c) an adequate source of test gas must be supplied for the range of adsorption phenomena to be studied.

A UHV system incorporating the above requirement has been fabricated. The system consists of a crystal chamber ( $1\frac{1}{2}$  in. dia. x 20 in. long) a specially designed coaxial vacuum feedthrough unit onto which the quartz crystal is mounted, gas inlet system and associated vacuum plumbing. This system is attached to the Partial Pressure Analyzer System (PPAS)<sup>1</sup> via a bakeable high conductance isolation valve (see Fig. 3). Not only are the UHV pumping facilities of the PPAS utilized but also the gas analysis capabilities. The entire system is bakeable to 400°C and can maintain a pressure of  $1 \times 10^{-9}$  Torr with only the 8 liter/sec getter-ion pump operating. Analysis of the residual gas in this system indicates that H<sub>2</sub> and CO are the major constituents and that all other gases have partial pressures below  $1 \times 10^{-10}$  Torr.

The temperature of the crystal is established by submerging the crystal zone (the lower 10 in. of the crystal chamber which is seen in the foreground of Fig. 3) into a dewar of cryogenic liquid. To avoid excessive boil-off of the cryogenic liquid, the lower 16 in. of crystal chamber is fabricated from thin-walled stainless steel tubing. The dewar mounting is such that a mechanical vacuum pump can be used to vary the pressure above the cryogenic liquid thus making some temperature variance possible.

The quartz crystal is mounted at the end of two specially designed coaxial leads as shown in Fig. 4. The coaxial leads are also fabricated from thin-wall stainless steel tubing with ceramic insulators at various positions along their 22 in. length. Outgassing slots have been cut in both the outer and inner tubes.

Figure 5 shows in detail the lower end of the coaxial leads. A platform is fixed between the outer tubes and supports a system of carefully positioned beryllium copper leaf springs which press against the tubular wall of the vacuum chamber. The springs are arranged in a spiral staircase configuration such that the array is optically dense, but maintains a high conductance value for gas flow. This assembly performs two functions: (1) it shields the crystal chamber from radiation from the warmer parts of the vacuum system, and (2) it conducts heat from the coaxial leads to the cryogenically cooled vacuum finger wall. The cryogenic liquid level is maintained at a point at least 2 in. above the spring assembly during data collection periods. Thus, in operation the crystal is surrounded by cold surfaces. Note the crystal does not cool as rapidly as the vacuum vessel walls which are in direct contact with cryogenic fluids. Therefore, when LHe, LH<sub>2</sub> or LNe are used contaminating gases are trapped on the vacuum chamber walls before the crystal can begin significant adsorption. For the results reported below LHe was used.

When the vacuum finger is cooled to LHe temperature and the isolation valve is closed (thus eliminating all pumps from the system except for the ion gauge and cryofinger) the pressure in the room temperature part of the system is  $1 \times 10^{-10}$  Torr or lower. Using a thermal transpiration correction it is determined that the pressure in the crystal zone is below  $1 \times 10^{-12}$  Torr. This pressure level for contaminating gases is sufficiently low to present no significant effect on the adsorption measurement. After an equilibrium condition is established for pressure, temperature, and crystal frequency a test gas is admitted to the crystal chamber. Since this study deals with the adsorption of helium onto liquid helium temperature surfaces, a 6 in. vycor diffuser is used for the gas inlet system (see Fig. 3, immediately above the PPA magnet). The pressure can be slowly raised in the system by gradually increasing the diffuser operation up to a maximum level of 0.1 micron liter/sec.

2. The electronic equipment requirements are determined by the following needs; (1) a 5 Mc system with which to operate the microbalance, and (2) a data detection and recording system.

A stable 5 Mc oscillator system has been reported by P. A. Simpson and A. H. Morgan.<sup>3/</sup> Based on their design a similar system was assembled for this set of experiments and a schematic diagram is shown in Fig. 6. Care was taken in the layout of components to shield one stage from another, as is shown by the dashed lines in the diagram. Basically the system consists of a 5 Mc crystal controlled oscillator circuit followed by a single stage amplifier which delivers a signal to an automatic gain control circuit (AGC) and to additional amplifier stages. The AGC supplies a feedback loop to the 5 Mc oscillator circuit. The additional amplifier stages supply output signals via a discriminator to a digital counter and a microamp meter. The meter is used to monitor the power required to operate the fundamental mode of the crystal. A detailed analysis of this circuit can be found in Ref. 3.

The 5 Mc crystals used in this study were obtained from AT cuts of synthetic quartz and have a 0.550 in. diameter. The edges of the crystal have a slight 20 diopter biconvex bevel. Figures 4 and 5 display a typical crystal mounted on the ends of the specially fabricated coaxial leads. An electrode is deposited on each side of the crystal and each electrode is connected to one of the coaxial leads via a spring clip unit. It has been determined that the crystals and the mounting units continue to function reliably after repeated exposures to the temperature extremes of the experiment, viz.,  $\sim 4^\circ\text{K}$  to  $673^\circ\text{K}$ . Silver and aluminum have been used as electrode materials. However, the silver electrodes are not satisfactory because electrical continuity is lost during initial operation. It has been determined that the failure occurs between the clips holding the crystals and the main body of the electrode.

Aluminum electrodes have been tested and found to be satisfactory throughout the entire operational range of pressure and temperature. It should be noted, however, that the effort on this study is not directed toward developing any particular electrode material or geometry. The only interest is to determine the value of the microbalance technique for cryopanel studies. It should be possible to use many conducting materials as electrodes including silver.

A summary of the data collection and recording system is given by the schematic diagram in Fig. 7. The system pressure is monitored by a Bayard-Alpert type gauge (BAG) i.e., a Varian UHV-12. Pressure data are fed from the gauge control unit to the y coordinate of any x-y plotter. The frequency at which the oscillator is operating is monitored by a digital counter which feeds frequency data to a digital to analog converter. The converter monitors the last three significant figures of the incoming data and generates a signal which is then fed to the x coordinate of the x-y plotter and to a strip chart recorder.

### C. Correlation of Adsorption Data with Theoretical Prediction

We now have the task of applying the TAL theory to the experimental results. The data for helium on aluminum are plotted in Fig. 8. To compare these data with the theory we must express the measured frequency,  $f$ , in terms of  $\theta$ . It is quite reasonable to assume that a linear relationship exists between  $f$  and  $\theta$ , i.e.,

$$\theta = k(f_0 - f) \quad (11)$$

where  $f_0$  is the frequency when there is negligible adsorption of the controlled gas. There may, at  $f_0$ , be many adsorbed layers on the pure surface but we only assume that the surface is energetically flat at  $f_0$  and will not be concerned with the actual composition of that surface. To evaluate  $k$  in Eq. (11) it seems reasonable, based on past experience, to assume that the first large hump in the experimental data signifies the completion of first monolayer. That is, we will assume that  $\theta = 1$  and the pressure ( $p$ ) and crystal frequency ( $f$ ) designations ( $p_1, f_1$ ) correspond to the completion of first monolayer adsorption for this point on the experimental curve. Then

$$k = \frac{1}{f_0 - f_1} \quad (12)$$

and

$$\theta = (f_0 - f) / (f_0 - f_1) \quad . \quad (13)$$

For the present case

$$f_0 = 5,000,994 \text{ cps before helium adsorption began}$$

$$f_1 = 5,000,718 \text{ cps}$$

and

$$p_1 = 1.024 \times 10^{-5} \text{ Torr for first monolayer coverage}$$

$$(\theta = 1) \quad (14)$$

These factors yield an experimental plot of  $\theta$  versus pressure. However, the most desired information from the experimental data is values of  $W_s$  and  $D$  since these are not well known (the values of  $\epsilon$  and  $\sigma$  can be reasonably approximated from their gas-gas interaction values<sup>4</sup>). The  $W_s$  value is easily determined by taking the limit of very small coverage in Eq. (8), i.e.,

$$W_s = T(\ln K + 1.5 \ln M + 2.5 \ln T + \ln s) \quad (15)$$

where  $s = \theta/p$  is the experimentally measured slope at very low coverages. For the present case  $s = 4.13 \times 10^7$  and the resultant Eq. (15) is shown in Fig. 9. Due caution must be exercised when using Eq. (15). It appears that  $W$  is a function of temperature but this is not true. Ideally, the variation in  $s$  should be just enough to cancel out any variation in the temperature. Figure 9 is presented only because, in our case, the temperature is unknown.

Although an experimental value for  $W_s$  is easily obtained from Eq. (15) without the need of a computer, the experimental value for  $D$  is more difficult to deduce. We assume that at  $p_1$  the value of  $\theta_1$  is 0.99, i.e., that  $\theta_2 = 0.01$ . An iteration process is then applied to Eq. (8) with  $j = 2$  to obtain a value of  $D$ .

Having a method for determining  $W_s$  and  $D$ , we should now like to determine the temperature. This can be done best by plotting the TAL theoretical isotherms for various temperatures and comparing them with the experimental isotherm. This has been done in Fig. 10 for temperatures  $6^\circ$  to  $20^\circ\text{K}$ . It is clear that the TAL curves for  $6 - 11^\circ$  give too much adsorption, whereas the TAL curves for  $12 - 20^\circ$  give too little. Employing an area under the curve method for data correlation, we see that the best fit lies close to  $12^\circ\text{K}$ . Since these curves are intended only to exhibit the feasibility of applying the theory to practical problems, no attempt was made to bring the experimental and TAL curves into coincidence by an adjustment of parameters. In fact, the values of  $\theta_1$  at  $p_1$ ,  $a$ ,  $\sigma$ , and  $\epsilon$  were not adjusted. Under these circumstances the agreement of theory with experiment is quite good.

The rough fit of the curves in Fig. 10 leads to several qualitative conclusions:

1. The temperature is between  $10^\circ$  and  $15^\circ\text{K}$ , perhaps around  $12^\circ\text{K}$ .
2. The value of  $W_s$  lies between  $217^\circ$  and  $342^\circ\text{K}$ , perhaps about  $290^\circ\text{K}$ . This agrees well with the value of  $342^\circ\text{K}$  which Halsey<sup>5/</sup> experimentally measured on glass.
3. The value of  $D$  lies between  $3.9$  and  $4.9 \text{ \AA}$ , perhaps about  $4.5 \text{ \AA}$ . This value does not agree with the value  $D = 1.9$  measured by Halsey<sup>5/</sup> as discussed in (7) below.
4. The failure of the TAL curves to give adequate adsorption at higher pressures indicates that the values of  $a$ ,  $\sigma$ , and  $\epsilon$  are not accurate. This can be seen by noting that near the surface  $W_{sj}$ , i.e., the He-surface interaction, is the main interaction, but it falls off as  $r^{-3}$  (see Eq. (5)). Thus it appears that in the second or third layer the main interaction becomes  $\epsilon$ , i.e., the He-He interaction. Although  $a$ ,  $\sigma$ , and  $\epsilon$  can be determined as  $D$  is determined, no attempt was made to adjust these values since the experimental data at a temperature near  $12^\circ\text{K}$  do not warrant such an extensive analysis of multiple layer adsorption.
5. The value of  $\sigma_s$  lies between  $4.6$  and  $5.7 \text{ \AA}$ . The gas-gas value for  $\sigma$  is  $2.6 \text{ \AA}$ .
6. The value of  $\epsilon_s$  lies between  $47^\circ$  and  $39^\circ\text{K}$ . The gas-gas value for  $\epsilon$  is  $10^\circ\text{K}$ .

7. The value of  $\epsilon_s$  indicates that the He-surface interaction is about four times stronger than the He-He interaction but is slightly weaker than that measured by Halsey. The high values of  $D$  and  $\sigma_s$  indicate that the first layer is considerably removed from the surface. These facts seem to indicate that the "surface" employed in these experiments is composed of at least one layer of adsorbed material over the aluminum oxide layer. This adsorbed layer would lower the  $W_s$  value from that measured by Halsey since he operated at much higher temperatures and presumably had no adsorbed layers on his glass surface. The adsorbed layer would also increase  $D$  and  $\sigma_s$  since the He-oxide interaction would be stronger than the He-adsorbed layer interaction but would be further from the first layer. The result is a lower "effective distance"  $D$ . This picture of an adsorbed layer on the oxide layer is, of course, quite reasonable and even to be expected at these low temperatures.

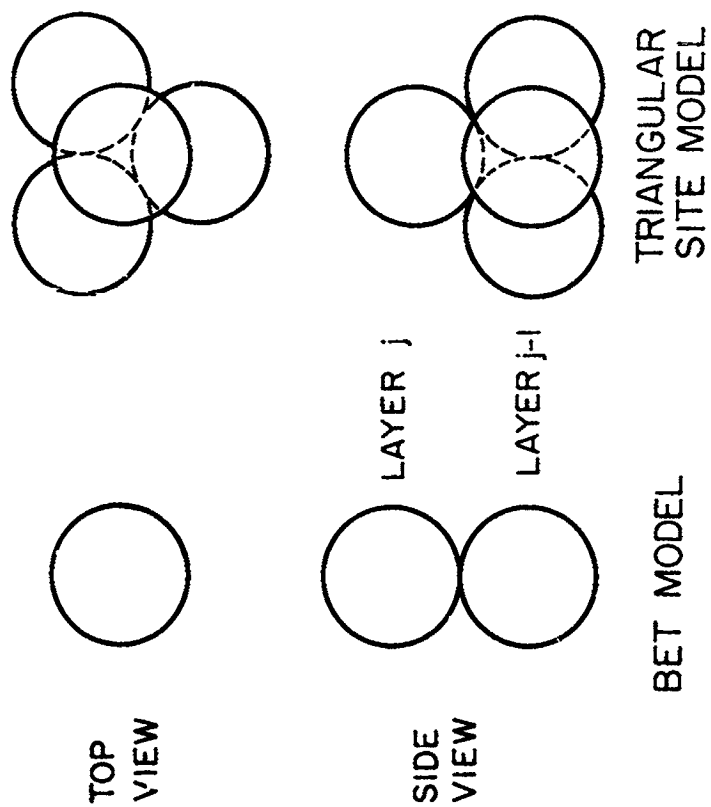


Fig. 1 - Adsorption Site Models for the Atomic Arrangement Used in the Development of the BET Theory (left) and Triangular Site Model (right).

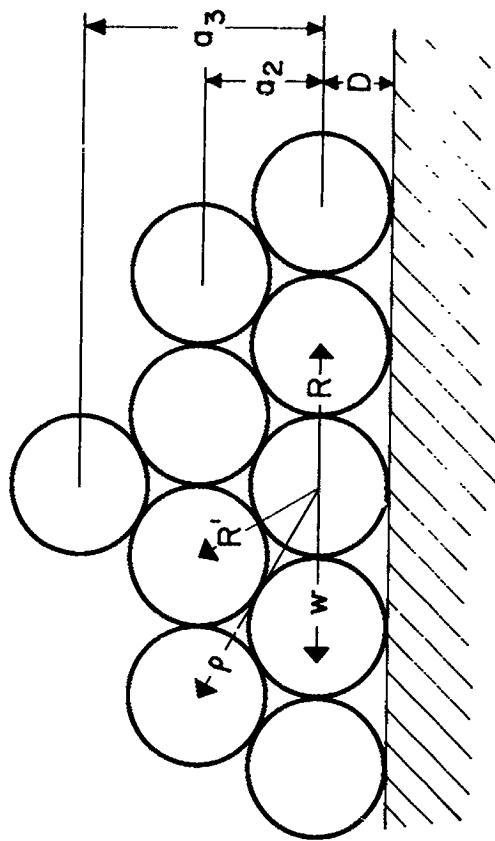


Fig. 2 - Adsorption Geometry for the Triangular Model Showing: Nearest and Next Nearest Neighbor, and Interlayer Spacings; and First Adsorbed to Adsorbent Spacing,  $D$ .

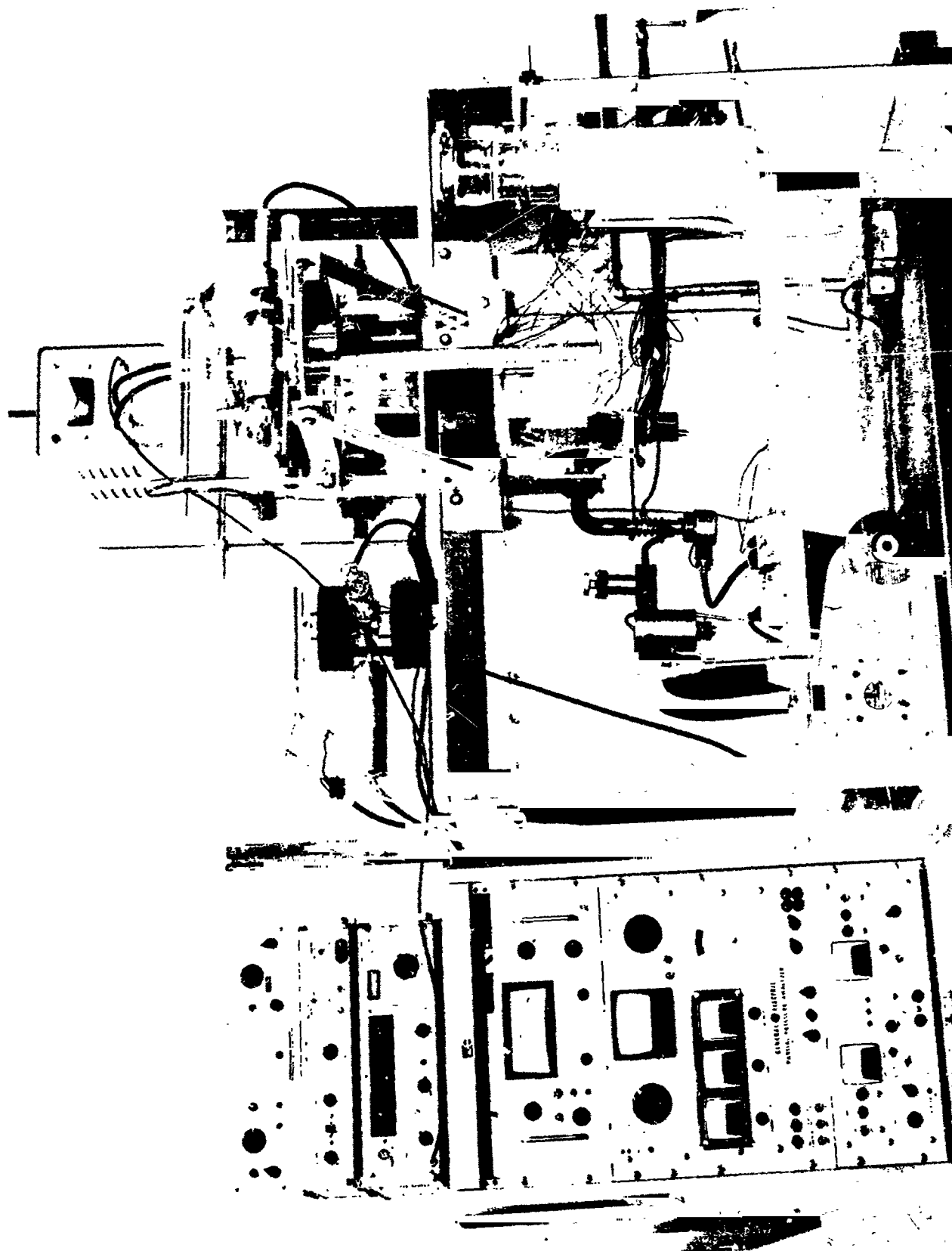


Fig. 3 - Microbalance System Attached to the PPAS. The Microbalance Environmental System Includes the Cryofinger (foreground) Containing Specially Designed Coaxial Leads and Crystal, Helium Diffuser (shown above electro magnet), and Associated Plumbing. The pumping station and PPAS are described in Refs. 1 and 5.

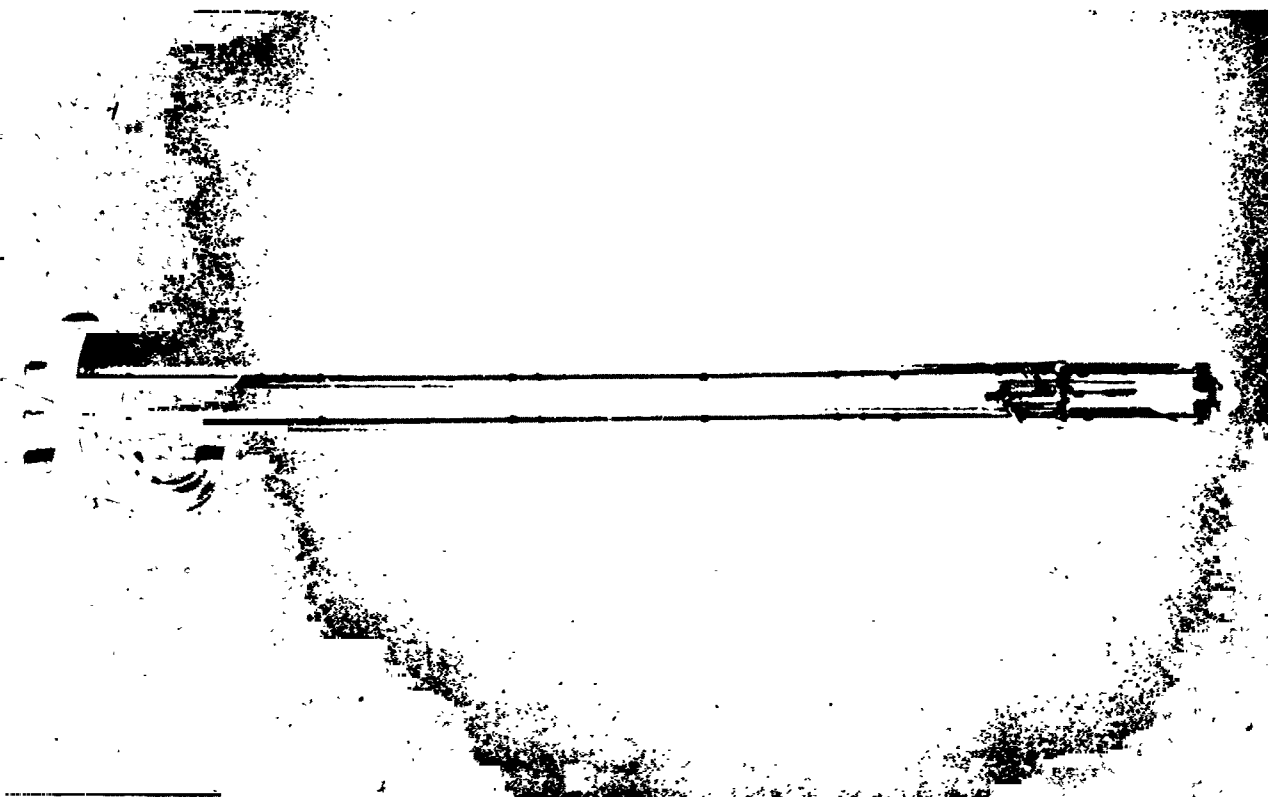


Fig. 4 - Coaxial Vacuum Lead Assembly on Which Quartz Crystals are Mounted. Leads are fabricated from thin wall stainless steel and have been slotted to insure thorough outgassing during bake periods.

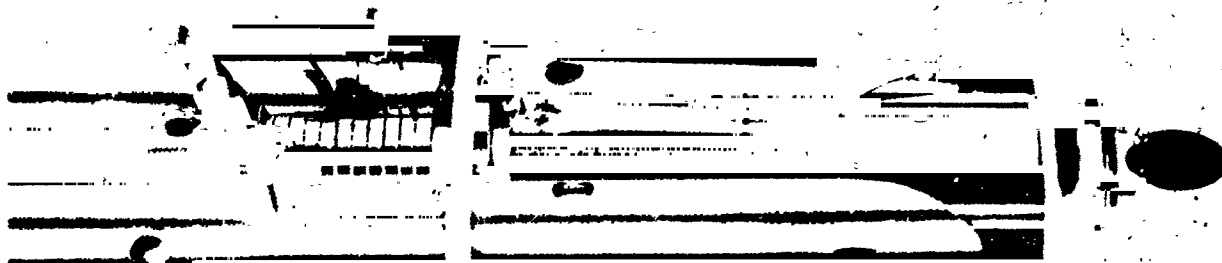


Fig. 5 - Lower End of Coaxial Vacuum Leads. A beryllium copper spring assembly establishes thermal conduction to the cryofinger wall and forms a radiation shield.



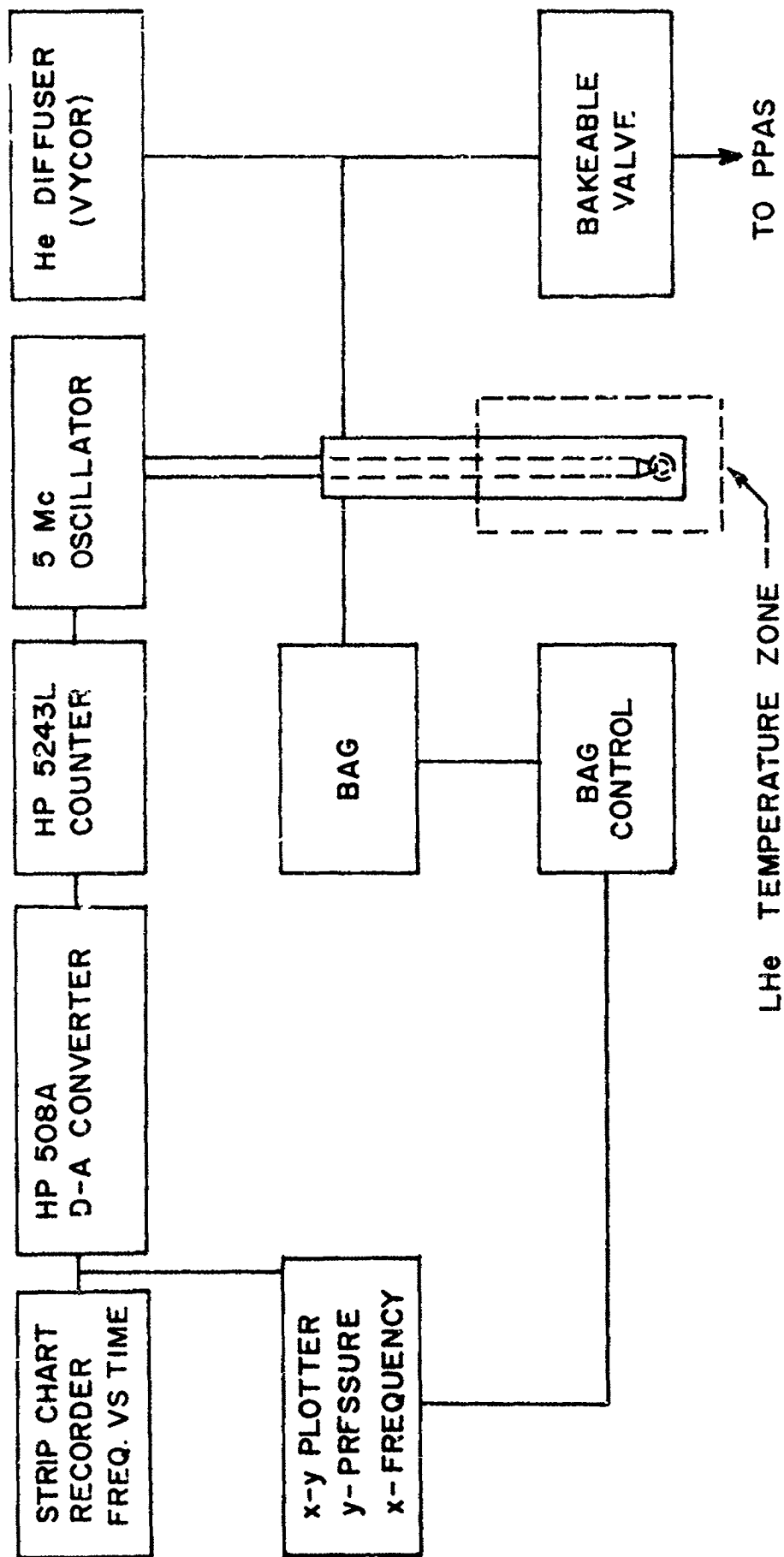


Fig. 7 - Schematic Diagram of the Major Electronic and Environmental Components Used with the Microbalance System. Gas pressure in the system is monitored by a Varian UHV-12 ion gauge (BAG) and plotted on the y coordinate of the x-y plotter. The crystal frequency shift is plotted on the x coordinate.

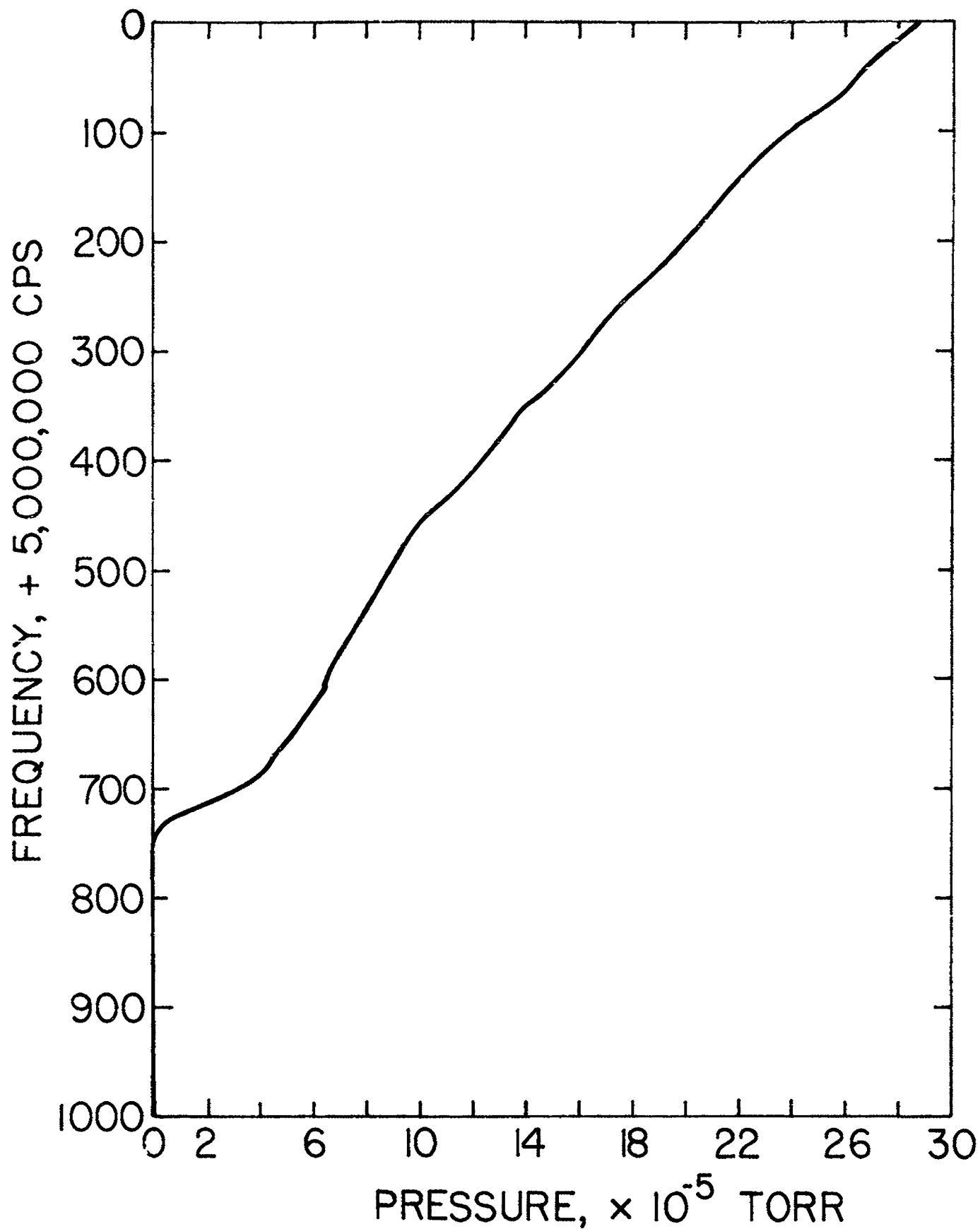


Fig. 8 - Experimental Data for Helium Adsorption on Aluminum Near 12°K; an Extremely High Sensitivity of about 200 Cycles/Monolayer is Indicated for the Piezoelectric Crystal Microbalance

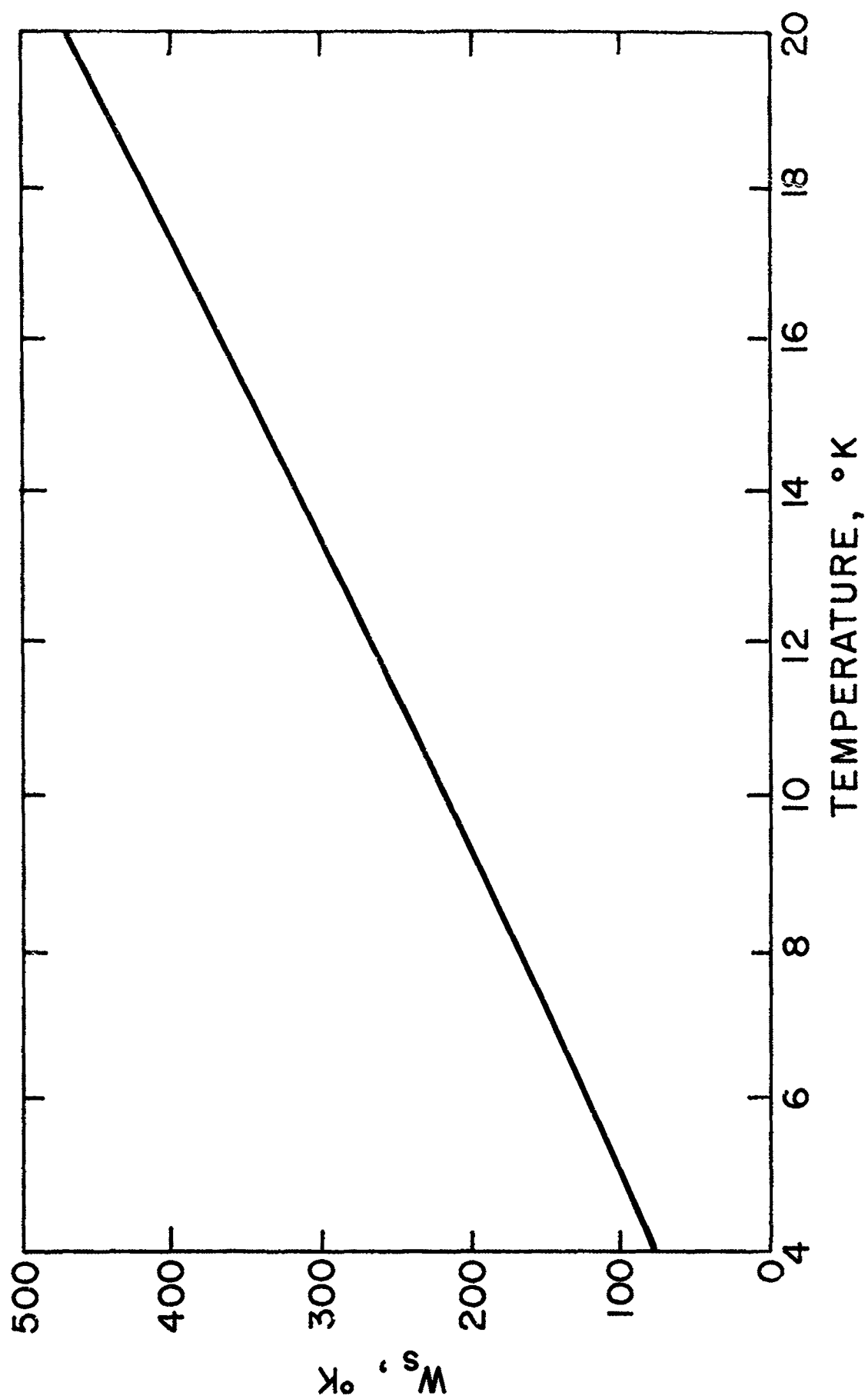


Fig. 9 - A Plot of the Surface Interaction Energy  $W_s$  as a Function of Temperature According to Eq. (15).

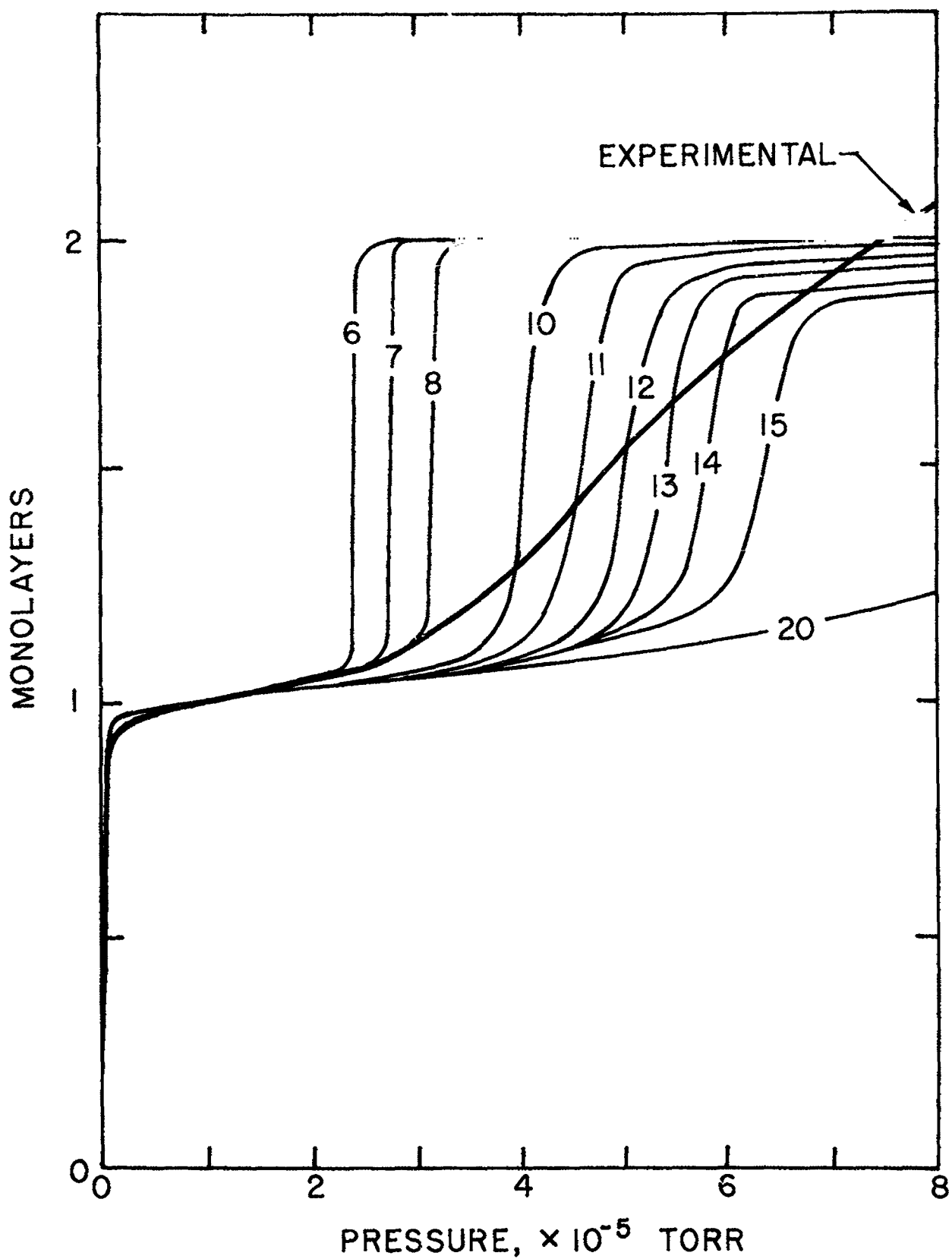


Fig. 10 - A Composite Plot of Experimental and Theoretical Adsorption Isotherms. Experimental results correlate best with the 12°K theoretical curve.

## II. EVALUATION OF A DUAL EXPANSION NOZZLE FOR IMPROVED DIFFUSION PUMP OPERATION

A dual expansion nozzle has been constructed and evaluated. This study has revealed that a significant increase in pumping speed can be maintained while operating at elevated boiler temperatures.

### A. Discussion of Diffusion Pump Operation

A literature review dealing with the mechanics of vapor jet pumping has already been presented.<sup>1,6/</sup> Also the main experimental equipment used in this study has been described<sup>1/</sup> and preliminary results have been given for a single jet nozzle.<sup>1/</sup> This report presents data collected for both a single jet and a dual jet design. Based on the data it is clear that a significant advantage can be gained from a dual expansion type nozzle.

The operation of a vapor pump will now be reviewed. The working fluid (Hg in this case) is heated in a boiler to increase the vapor pressure in the jet stack and to impart kinetic energy to the evolving gas. The pump vapor then flows through a tube to a nozzle assembly where it undergoes an expansion into a pumping region thus forming a vapor jet. The geometry and orientation of the jet is such that the pump vapor collides with a cold surface, where it condenses. This condensate is then returned to the boiler assembly for recirculation.

The pumping effect of this recycling vapor flow is based on a transfer of momentum from the expanding jet to (1) gas molecules which are back diffusing through the jet region into the vacuum chamber, and (2) incoming molecules from the vacuum chamber. The vector sense of the momentum transfer is such that the direction of gas flow is established away from the vacuum chamber.

The first process of limiting back diffusion determines the pressure drop which can be maintained across the vapor jet. This process is highly dependent on the vapor density, viz, higher density jets can maintain a greater pressure differential.

The second process, molecule entrainment by the vapor jet, determines the pumping speed. The critical parameter in this function is the degree of uniformity with which the momentum is transferred from the vapor jet to incoming gas molecules. This is particularly true at the upper boundary of the jet where the incoming gas first encounters the vapor stream. If there

is turbulence at this boundary, significant amounts of gas can be repelled back into the vacuum chamber. The amount of such turbulence is a function of nozzle design and vapor density<sup>6/</sup> viz., lower density jets generate less turbulence.

A dilemma arises when back diffusion is reduced by increasing boiler pressure, because the corresponding increase of turbulence in the vapor jet reduces the ability to entrain gases. It has been postulated that a dual expansion nozzle would aid in resolving the dilemma<sup>7,6/</sup>. Such a nozzle should generate a high density main jet surrounded by a low density umbrella jet. Therefore, it is the purpose of the present work to determine the relative pumping efficiency of a dual expansion nozzle versus a single expansion nozzle when operating at high boiler pressure.

A schematic diagram of the nozzle assembly designed for this work is shown in Fig. 11. This assembly consists of a movable end cap which is used to form a low density umbrella jet, and a fixed deflection skirt used to form the main high density jet. The thin-walled stainless steel tube which supports the end cap is attached to a screw driving assembly outside the vacuum system via a bellows in the bottom of the mercury boiler, as shown in Fig. 12. This tube can be used to increase or decrease the gap between the end cap and the top of the jet stack. The gap was opened to 0.010 in. when the nozzle was used in the dual expansion mode. The temperatures at the boiler and various positions along the jet stack including the exit aperture at the nozzle is monitored by a series of thermocouples which have been inserted into the thin-walled stainless steel tube. The boiler-jet stack unit as described earlier<sup>6/</sup> has been modified. The main body of the boiler assembly has been lengthened by 3 in. to establish a thermal barrier (an evacuated region) between the hot assemblies, boiler and jet stack, and the cooler region, mercury accumulator ring and return line (see Fig. 12).

Minor component changes have also been made in the over-all vacuum system. However, the basic operation and measurement techniques are the same as presented earlier.<sup>1/</sup> Figure 13 displays the present system configuration.

Two experimental measurements are of interest as a function of vapor jet density or boiler temperature;

1. The pump speed of the nozzle assembly for the two modes of operation, i.e., with and without an umbrella jet, and
2. The ratio of pressures which can be maintained across the jet region.

The pump speed determination is based on the following calculation:

$$S = \frac{Q}{P_1} \quad (16)$$

where  $S$  = pump speed,  $Q$  = gas flowing into the system, and  $P_1$  = pressure in the system. The gas flow through a conductance  $C$  is given by the equation:

$$Q = C(P_2 - P_1) \quad (17)$$

where  $C$  = conductance of the orifice,  $P_2$  = pressure at gauge 2, and  $P_1$  = pressure at gauge 1 (see Fig. 13). Substituting Eq. (17) into Eq. (16) gives:

$$S = C \left[ \frac{P_2}{P_1} - 1 \right]. \quad (18)$$

The conductance ( $C$ ) is determined by

$$C = 3.638 KA \left( \frac{T}{M} \right)^{1/2} \text{ liters/ sec} \quad (19)$$

where  $K$  = Clausius or variational factor,  $A$  = cross-sectional area of the orifice ( $\text{cm}^2$ ),  $T$  = temperature ( $^{\circ}\text{K}$ ), and  $M$  = gram molecular weight of the flowing gas.

Helium is used as the test gas in these measurements, therefore  $M = 4$ . This gas is supplied via a 6-in. vycor diffuser which is mounted close to the orifice ( $C$ ). The heat generated when operating the diffuser establishes an orifice temperature of  $455^{\circ}\text{K}$  during the test. The area ( $A$ ) of the orifice is  $0.148 \text{ cm}^2$  and  $K = 0.5814$ . Substituting these values in Eq. (19),  $C$  is determined to be:

$$C = 3.34 \text{ liters/sec} *$$

---

\* See Ref. 1 for data at other temperatures and masses.

Finally, Eq. (18) can be written as

$$S = 3.34 \left[ \frac{P_2}{P_1} - 1 \right] \text{ liters/sec} .$$

The ratio of pressures maintained across the jet region is also calculated for the range of boiler temperatures studied. Helium is again used as the test gas; however, a larger source is required because of the pumping speed of the two-stage backing diffusion pump. Therefore, a large quartz diffuser is used to supply up to 1 micron liter per second of pure helium.

## B. Results and Conclusions

Data are presented graphically in Figs. 14 and 15 for both the umbrella and nonumbrella jet configurations. The boiler temperature was varied slowly between 24°C to 232°C. However, above 197°C severe pressure fluctuation occurred and quite often the electronic protection circuits would shut off the gauges. Therefore, no data are presented for this unstable operating range. The data below approximately 115°C show the effect of the two stage diffusion pump which backs the test chamber (see Fig. 13). Above this temperature the vapor jet begins to form and intensifies with increasing boiler pressure. The pump speed for the configuration without an umbrella peaks near 170°C and subsequently falls off. In this region (170°C) the density of the gas has increased to the point where the Reynolds number has exceeded a critical value and, therefore, a turbulent flow has been established within the jet. Note that the peak pumping speed for the umbrella configuration is at about the same boiler temperature as for the nonumbrella situation; however, the peak has a greater value and does not fall off in the range presented. This behavior can be explained by noting that the umbrella jet has not yet reached a density sufficient to set up a turbulent flow condition; therefore, incoming gases are initially interacting with a more uniform flow condition than would be encountered if they interacted initially with the main jet.

The desirability of operating the main jet at a density corresponding to a turbulent flow condition can be deduced from the pressure ratio curve. At boiler temperatures below 195°C, the pressure ratio which can be maintained across the jet region has not yet peaked for either nozzle configuration. Therefore, to minimize the back diffusion of gases from the high pressure side of the vapor pump, the boiler temperature must be above the critical temperature corresponding to a turbulent flow in the main jet stream. However, the over-all pumping speed can be maintained if a low density umbrella jet is established over the main high density jet. That is, the dual expansion nozzle has shown significant improvements over the single nozzle design.

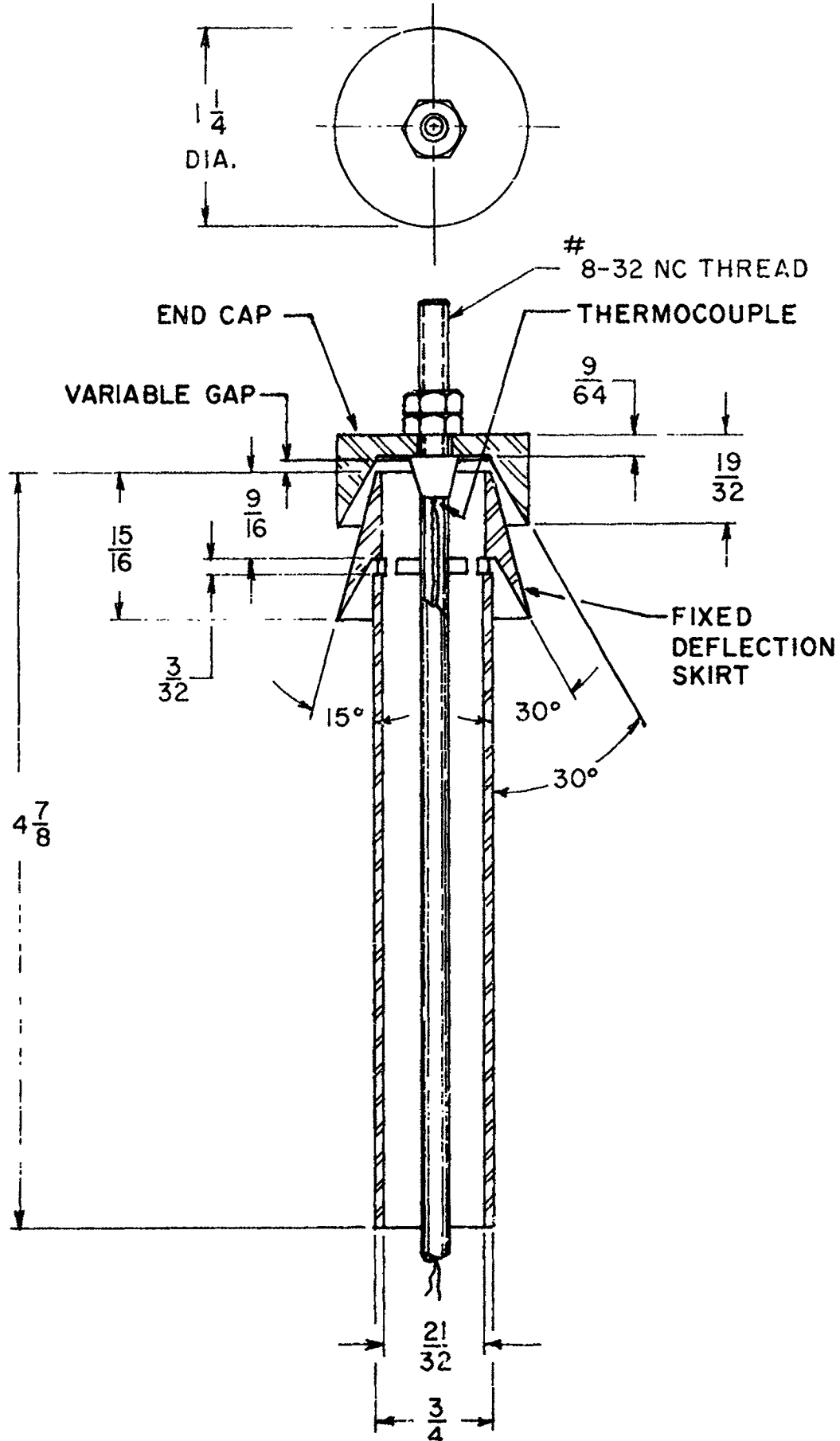


Fig. 11 - Schematic Diagram of a Dual Expansion Nozzle Assembly. An umbrella jet can be formed or eliminated by opening or closing the gap between the main assembly and the adjustable end cap.

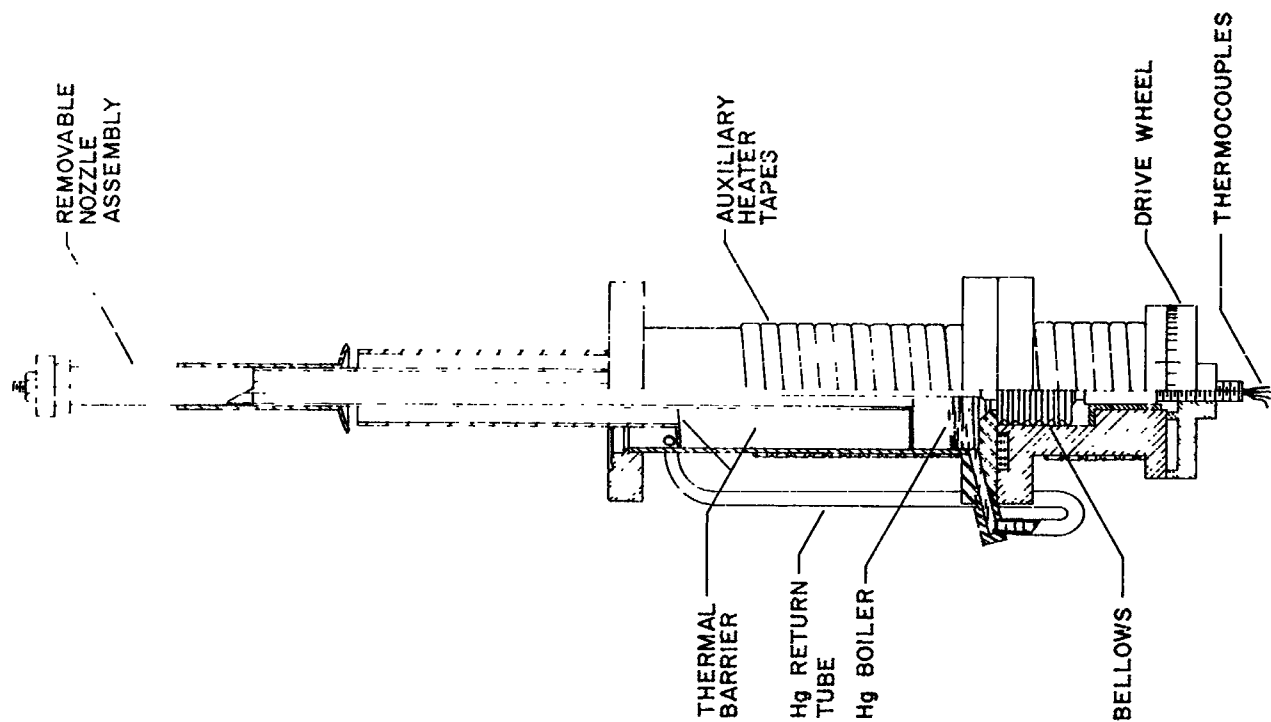
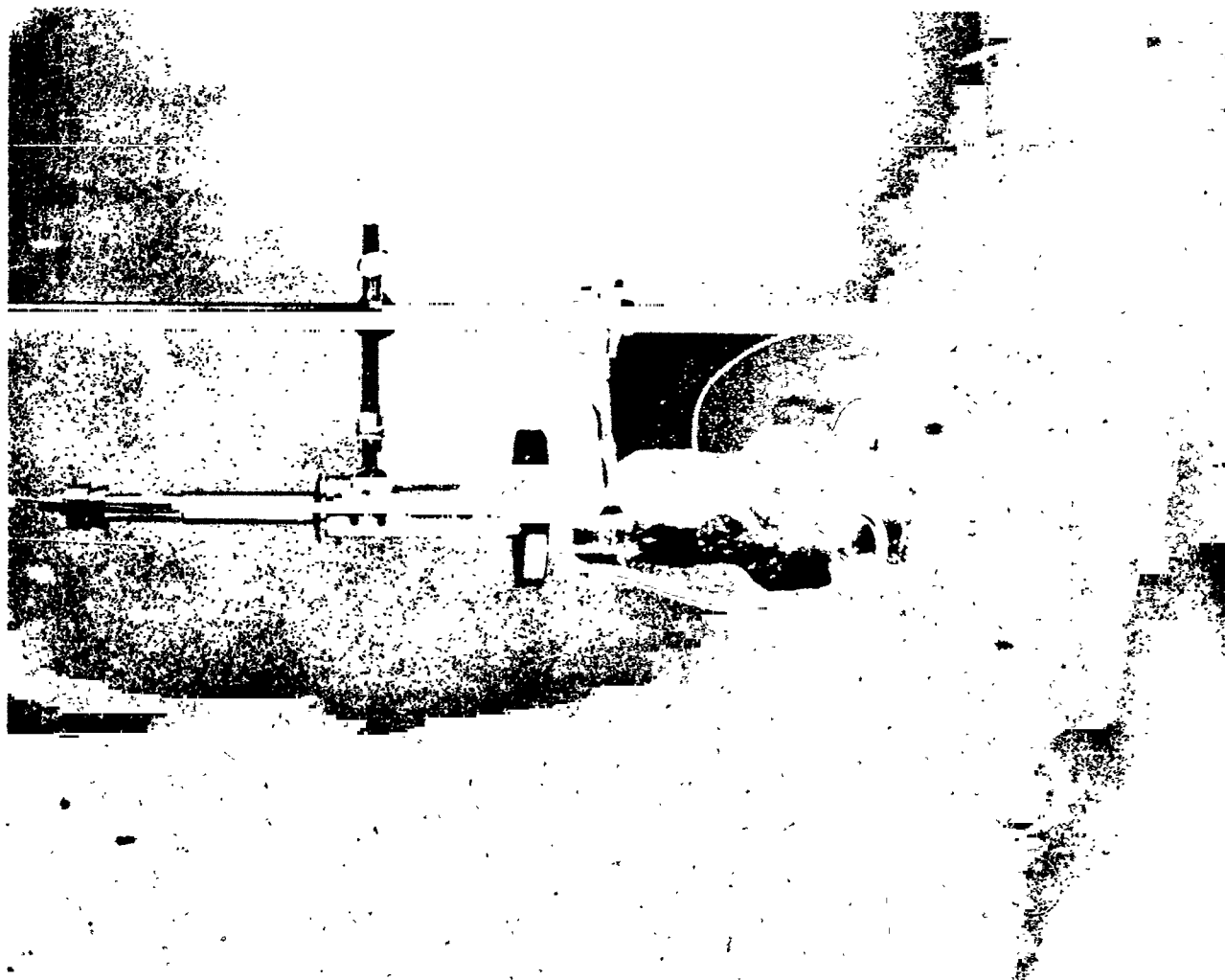


Fig. 12 - Schematic Diagram (right) and Photograph (left) of the Special Test Apparatus (modified) for Evaluation of Dual Expansion Diffusion Pump Nozzles. The drive mechanism provides for continuous variation of nozzle gap during operation.

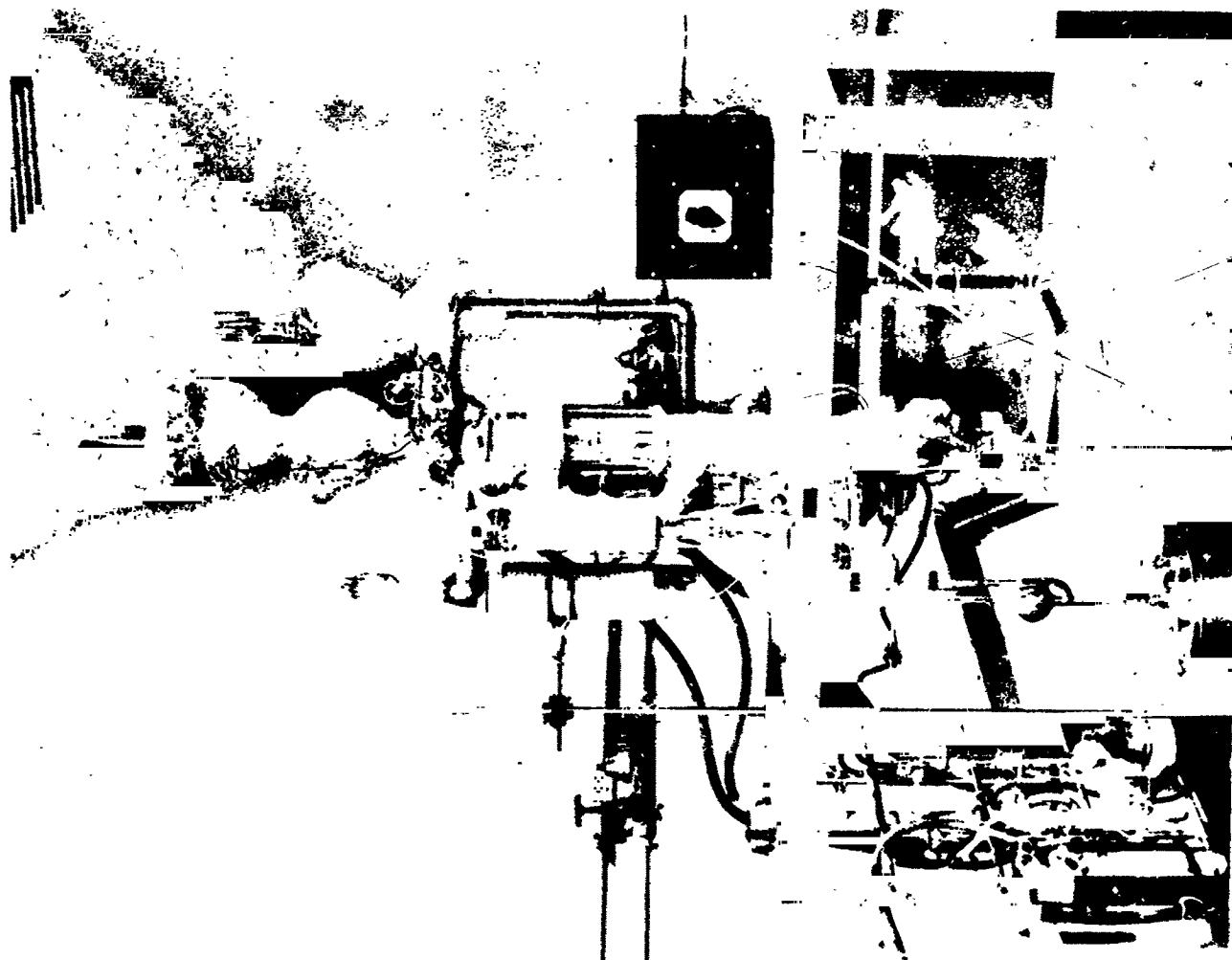
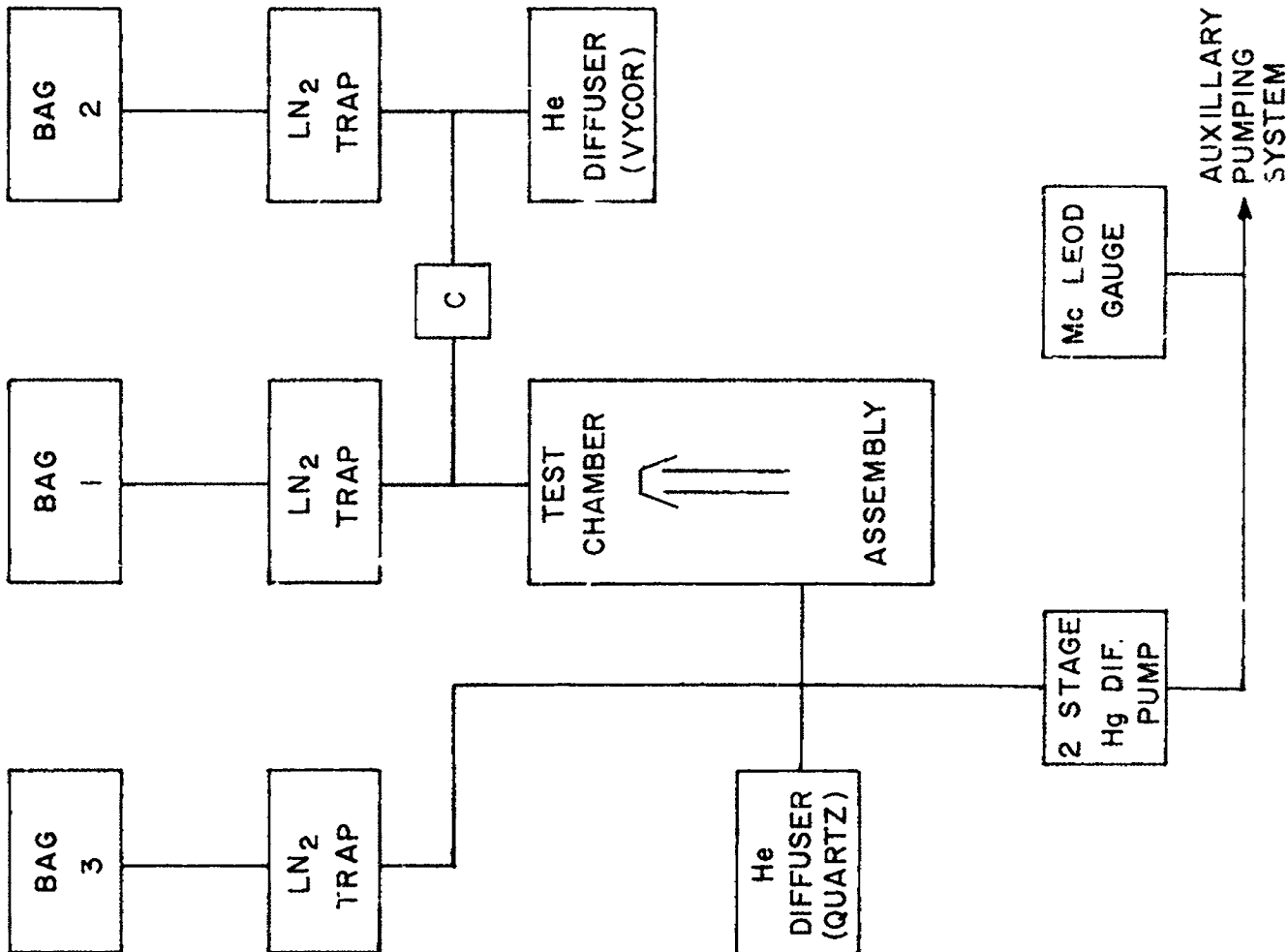


Fig. 13 - Schematic Diagram (right) and Photograph (left) of the Vapor Jet Test System. The special test apparatus (in Fig. 12) is shown mounted in test chamber assembly.

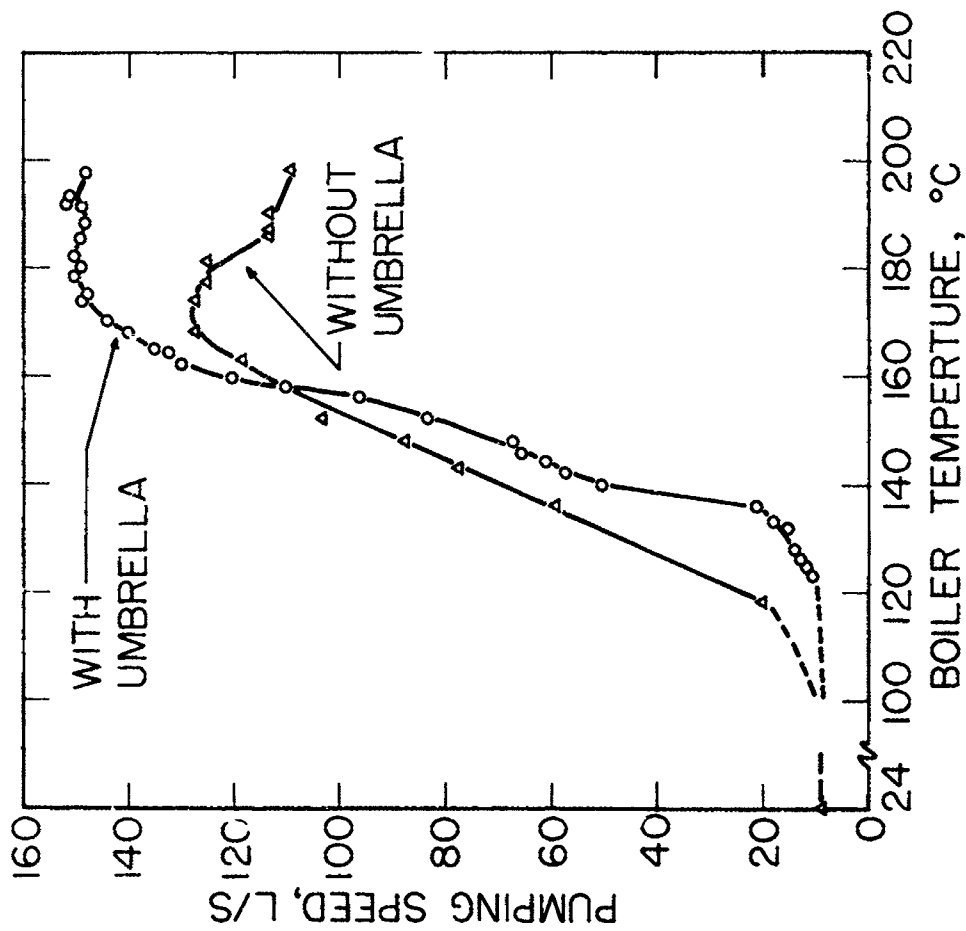


Fig. 14 - Graph of the Pumping Speed for a Single and Dual Expansion Nozzle as a Function of Boiler Temperature. For the single expansion nozzle, pump speed rises with boiler temperature to 175°C and then begins to fall off, whereas for the dual expansion nozzle, an increased pump speed is maintained to a temperature of 200°C.

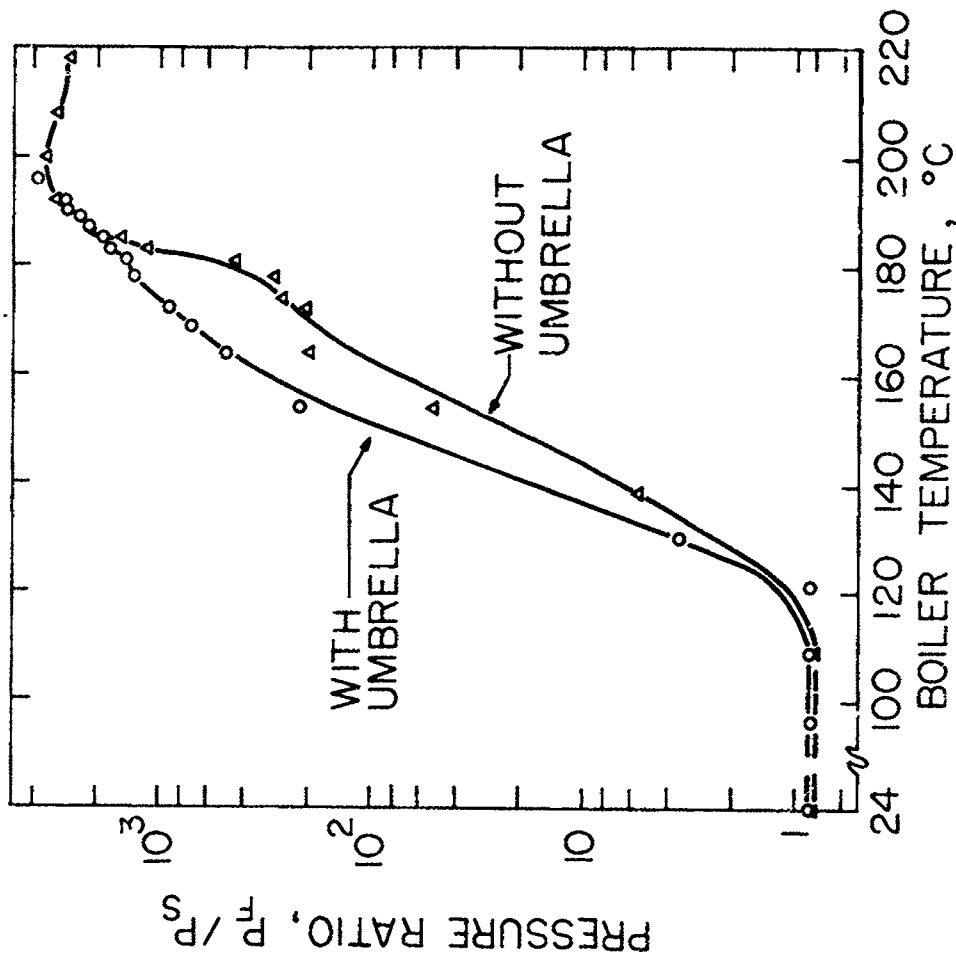


Fig. 15 - Graph of the Pressure Ratio Maintained Across the Jet Region for Both a Single and Dual Expansion Nozzle as a Function of Boiler Temperature. Note that the maximum pressure ratio has been established at 195°C.

### III. EXTREME VACUUM MEASUREMENT TECHNIQUES INCLUDING A FIELD EMISSION MICROSCOPE STUDY

A description of cold cathode magnetrons and Penning cells operating as gauges has been developed in terms of the conditions for establishing a discharge and the effects of space charge buildup. Pressure response curves for three commercial gauges (Redhead, Kreisman and trigger discharge types) were determined by a conductance-regulated, pressure-ratio method using Bayard-Alpert type gauges for reference.

Four characteristics are predicted for magnetrons from a consideration of the discharge mechanism and from a correlation with test data: (1) an out-of-strike state characterized by a steady pressure-independent background reading of about  $5 \times 10^{-14}$  Torr; (2) a minimum pressure threshold for operation ( $2.7 \times 10^{-12}$  Torr for Redhead,  $1.7 \times 10^{-10}$  Torr for Kreisman); (3) a range of nonlinear pressure-dependent response above threshold in which the sensitivity rise with pressure is moderated by space charge buildup; followed by (4) a range of near linear response (slope of 1.04 for Redhead, 1.11 for Kreisman types on a log pressure-log current plot) corresponding to the region of nearly saturated space charge. Differences in response values are correlated with differences in electrode elements, spacings, and voltages for the two magnetron gauge tube designs.

Response characteristics have been determined for G.E. trigger discharge gauges. Four characteristics have been identified from test data and described in terms of the discharge process: (1) a pressure insensitive state below  $10^{-11}$  Torr in which the predominant current is due to either leakage, field emission, or a combination thereof; (2) a pressure-dependent increase of ion current above  $10^{-11}$  Torr; (3) a discontinuous jump (by a factor of about 2 in ion current near the  $10^{-9}$  Torr range corresponding to the establishment of an electron cloud virtual cathode, and the conversion to a magnetron type discharge which increases nonlinearly with pressure but with space charge moderation along a 1.15 slope; and (4) a saturation phenomenon near  $10^{-4}$  Torr due to the establishment of a glow discharge and ion recombinations.

#### A. Cold Cathode Gauge Operation Based on a Magnetron Type Discharge

A Penning type discharge cell<sup>8/</sup> generally consists of a cylindrical or rectangular anode cage with two end plate cathodes which are not concentric with the anode. The G.E. trigger discharge gauge<sup>9/</sup> employs a 1/2-in. Penning type cell with some modifications such as a cylindrical rather than a C-shaped magnet and small holes in the end plates for the passage of electrons from a filament mounted just outside of the cell. The operation of a Penning cell

such as used in the trigger gauge is similar to that of a magnetron since the electron cloud forms a virtual cathode concentric with the anode. This report therefore concentrates upon the description of magnetron type discharges. Section A below presents a history and discussion of gaseous discharges as applied to cold cathode vacuum gauge operation.

A magnetron may be defined as an assembly of two concentric cylindrical electrodes operated in an axial magnetic field. When used as a pressure gauge, the electric and magnetic fields are chosen such that the bulk of the cavity is beyond magnetron cutoff. That is, electrons are not able to travel from cathode to anode unless they lose energy by colliding with gas molecules (see Fig. 16). The gauge, therefore, remains in an out-of-strike state, unless the gas pressure is high enough to support a discharge. The present report investigates this phenomenon as well as the basic operation of magnetron gauges. There are two commercially available gauges which may be described as magnetrons: the NRC Redhead gauge and the GCA Kreisman gauge.

In 1952, Beck and Brisbane<sup>10/</sup> reported a series of experiments using both normal and inverted magnetron arrangements. A central wire and a cylinder with several bulkhead discs were employed as electrodes. The sensitivity was high when used as an inverted magnetron. The device had two disadvantages: a background current due to field emission, which was equivalent to about  $10^{-8}$  Torr; and a power law rather than a linear relation between cathode current and gas pressure. However, a useful gauge circuit was designed using proper resistance values and a nonlinear meter scale.

Haefer<sup>11/</sup> developed a magnetron for an investigation of striking characteristics of a gaseous discharge in transverse electric and magnetic fields. The magnetron was found to strike at pressures below the sustaining discharge level for Penning cells designed up to that time. Much of the existing theory of magnetron gauge operation has been adapted from Haefer's work, which was based on the assumption of a negligible space charge and a uniform electric field. The first assumption holds only prior to striking, and the second does not hold for the electrode arrangements used in pressure gauges.

The next advance in magnetron pressure gauges was made by Hobson and Redhead.<sup>12,13/</sup> They eliminated the recording of erroneous field-emission current from the cathode by inserting auxiliary cathodes into an inverted magnetron structure. These additional electrodes shield the main cathode from the anode. Field emission from the auxiliary cathodes is independent of the ion current recording circuit. Thus an erroneous background reading was avoided. However, the linear response which Beck and Brisbane<sup>10/</sup> had predicted for operation near 2500 gauss was not obtained.

Redhead<sup>14/</sup> also designed a modification of the normal magnetron structure with cathode endplates in contact with the central cathode bar and with large rings as auxiliary cathodes (Fig. 17). Thus field emission was again removed from the ion current measuring circuit. A response near linearity ( $46^\circ$  slope on a log current -- log pressure plot) from about  $5 \times 10^{-10}$  Torr to  $10^{-3}$  Torr, and a departure from linearity ( $59^\circ$  slope) below  $5 \times 10^{-10}$  Torr, was found. At extremely low pressures, additional photoelectric action was necessary to insure starting. Using this modified design, Hobson<sup>15/</sup> reported a limiting pressure measurement of  $1.5 \times 10^{-12}$  Torr in a liquid helium-cooled system. The limit was assumed to be due to helium permeation through the walls of the glass system. The data actually appear to be the first published<sup>15/</sup> indication of the threshold phenomenon as described in this report.

Kreisman has devised several versions of cold cathode normal magnetrons<sup>16,17,18/</sup> placed in metal envelopes to avoid a breakage problem. One of these models<sup>18/</sup> (GCA 1410), which does not employ auxiliary cathodes (see Fig. 17), is available commercially. Also, the NRC magnetron gauge design was modified for flight tests<sup>18/</sup> by removing the auxiliary cathodes; a significant alteration of response occurred, as described later.

Rutherford's results<sup>10/</sup> on the behavior of Penning cells at low pressures show a large change of sensitivity as evidenced by a change of operating mode. These data for Penning cells are similar to the behavior of magnetron gauges at low pressures as reported here. However, the description<sup>9/</sup> of a triggered Penning cell does not report a similar response.

In this report, the expected characteristics of a magnetron gauge, with the space charge necessary to operate as an ionization gauge are discussed. Then a pressure-ratio technique used to test commercial magnetron gauges is described. The quantitative results of these tests are correlated with the qualitative features expected for space charge limited operation. The pressure response curves are then compared with the design features of the regular Redhead gauge, incorporating auxiliary cathodes, as well as with a special flight gauge and Kreisman design, both without auxiliary cathodes.

Jepsen<sup>21/</sup> has developed a theory which gives extensive consideration to the existence of a fully developed space charge of uniform density in both normal and inverted magnetron arrangements. The present consideration of space charge buildup with increasing pressure is treated qualitatively since the electron loss mechanisms are not well known. The basic electron loss mechanism has been assumed to be their arrival at the anode after several collisions. In the extremely high vacuum range, orbital lifetimes of electrons traveling from cathode to anode may extend to hours,<sup>11,13/</sup> if electronic oscillations do not interfere. When the cycloidal behavior of the electrons is considered, these long lifetimes and the velocity differences of the electrons could lead,

for example, to slipping stream instabilities which could return some electrons to the cathode and send others to the anode without the electron-molecule interactions postulated in the Townsend discharge theory.

Redhead has further investigated<sup>22/</sup> the "region of instability" reported earlier.<sup>14/</sup> Two operating states are reported for magnetic fields above and below a critical value. RF oscillations were found in the higher field state and sporadic noise in the lower or normal state. The maintenance of a maximum value of space charge was found in the linear response region. These important discoveries<sup>22/</sup> emphasize the role of space charge effects upon magnetron operation.

The qualitative picture of space charge moderated operation of a magnetron gauge will now be given. At sufficiently low pressure, electron loss mechanisms exceed the pressure dependent source of electrons to preclude the maintenance of a discharge. However, a background current (due to insulator leakage) gives an indicated pressure reading. These low pressure indications are not affected by removal of the magnet, a fact which confirms the lack of ion current in this cutoff state.

Electrons emitted from the cathode will describe short cutoff orbits starting from and ending on the cathode. (As Redhead<sup>14/</sup> indicates, these paths can cover a significant part of the cathode-anode distance.) However, the electron density in the gauge volume will be negligible until the number of electron-molecule interactions becomes significant.

For pressure values above a lower operating threshold, there are enough gas phase collisions to release electrons to cathode-independent paths at a rate which exceeds the total loss rate. A space charge then begins to build (see Fig. 16). The ions produced are detected at the cathode and the electrometer reading will change rather suddenly from a steady background value to a threshold ion current plus background reading when the discharge strikes.

As the space charge increases, the secondary electrons caused by ion bombardment of the cathode cylinder will see a lower electric field; and, although the number should increase with increasing ion current, the maximum kinetic energy in a complete cycloidal arc and the arc length will be reduced. The increase of space charge may eventually lead to a complete inactivation of the central portion of the cathode as an electron source. Thus, the cathode endplates or cones (Fig. 17) become increasingly important in defining the gamma coefficient for the discharge as pressure increases.

Finally, the electron space charge saturates and becomes nearly pressure independent so that a near constant gas ionization probability is maintained for further pressure rise. Thus the basically pressure-dependent discharge is constrained by saturation to be constant and produce a linear ion current to pressure response. The onset of this desirable feature near  $10^{-9}$  Torr defines the transition from nonlinear to linear response.

In summary, we would expect magnetron gauge operation to exhibit the following characteristics as pressure rises: (1) absence of a discharge below some low pressure level; (2) a threshold ion current at a pressure-dependent on gauge geometry and voltage; (3) a greater-than-linear rise of ion current with pressure due to the pressure dependent rise of the electron density itself; and (4) a saturated electron space charge (above about  $10^{-9}$  Torr) giving a linear ion current to pressure response.

#### B. Response Curves for Redhead, Kreisman, and Trigger Discharge Gauge Types

The characteristic response of ion current to pressure for cold cathode magnetron gauges was determined by a conductance-regulated, pressure-ratio method.<sup>23/</sup> This technique provided continuous operation of a reference Bayard-Alpert type hot-filament ionization gauge (BAG) located at a pressure two orders of magnitude above the pressure at the test magnetron gauge position.<sup>1/</sup> Thus the linear response of a BAG with constant emission current was used to obtain a continuous plot of the response curve for the magnetron gauges without the necessity of lowering the BAG to the level of residual collector current. The constancy of the pressure ratio was confirmed by using two BAG tubes on either side of the known conductance. Of course, the downstream BAG was then required to operate to a pressure below the X-ray photo current value. When corrections for total residual current were made (using the modulation technique<sup>24/</sup>), changes of the downstream gauge were found to remain linear with changes of the upstream gauge within gauge reading error.

The characteristic current-to-pressure response for G. E. trigger, NRC Redhead, and GCA Kreisman gauges was determined to their lowest operating values. The pressure-ratio method was employed for each gauge type. In addition, the Kreisman gauges were studied by direct comparisons to BAG, since the commercial BAG type employed (Varian model UHV-12) covers the full operating range of the commercial Kreisman gauge. The response curve for Kreisman gauges determined by direct comparison, with corrections for residual current in the BAG readings, agreed with the response curve obtained by the pressure ratio method. No correction for residual current in the BAG was required for the set of pressure ratio data, since the two order-of-magnitude ratio permitted operation to the low pressure limit of the Kreisman gauge without operating the BAG below  $10^{-8}$  Torr.

Output currents from the BAG, used as reference gauge, and the cold cathode gauges were simultaneously plotted on a uniform time base, established by operating a two-channel, strip-chart recorder using the recorder output terminals from the commercial control units. Ion currents and background currents were measured with a Cary model 35 vibrating reed electrometer. High voltages were set at the specified values of 4,800 volts for the Redhead type, 4,000 volts for the Kreisman type and 2,000 volts for the G. E. trigger type and regularly monitored with a sensitive Electrostatic Voltmeter. Magnetic field strengths of the permanent magnets were also checked periodically with a gauss meter and found to remain near the specified values. The BAG tubes (Varian model UHV-12) were operated with a grid potential of 130 volts, and an emission current of 4 ma, so that the sensitivity was 25/Torr. Therefore, all operating parameters were carefully maintained at the values specified by the manufacturers of each type gauge tube.

The characteristic response curves, determined from a large amount of data using the methods described above, are plotted in Figs. 18 through 23. Actual pressure values in dry air equivalent are plotted on the abscissae, and indicated pressures from the cold cathode gauge control units are plotted on the ordinates. Ordinate values may be converted to ion current values by multiplication with the dry air sensitivity factors (4.5 amps/Torr for the NRC 552 gauge, 2.0 amps/Torr for the GCA 1410 gauge and 2.5 amps/Torr for the G. E. trigger discharge gauge), since the control unit circuits (NRC 752, GCA 1400, and GE 22GC 201) are designed on the assumption of linear response, i.e., constant sensitivity.

The ultrahigh vacuum portion of the response curve for NRC Type 552 glass envelope (Redhead) gauges (Fig. 18) shows the following characteristics: (1) a background leakage current corresponding to an indicated pressure reading of  $5 \times 10^{-14}$  Torr when the real pressure is below the threshold for operation; (2) a total current value of  $9 \times 10^{-13}$  amp for initiation of a sustaining discharge; this threshold level corresponds to an indicated pressure of  $2 \times 10^{-13}$  Torr and a real pressure of about  $2.7 \times 10^{-12}$  Torr; (3) a non-linear response curve for values above threshold with a continuously changing slope approaching linearity near  $10^{-9}$  Torr; this is presumably due to the continuous buildup of space charge toward a saturated value, i.e., the sensitivity of the gauge increases as space charge increases until a nearly saturated state is reached at  $10^{-9}$  Torr; (4) a region of instability or resonance around  $7 \times 10^{-10}$  Torr characterized by oscillations in the output current; and (5) a response curve above  $10^{-9}$  Torr which has a nearly linear slope of 1.04 with a slow rise in sensitivity, due to additional buildup of the essentially saturated space charge. The  $46^\circ$  slope reported by Redhead<sup>14</sup> for the response curve above  $10^{-10}$  Torr is essentially identical to the value given here. The data below  $10^{-10}$  Torr agree closely with the data points given by Feakes and Torrey,<sup>25</sup> except for two differences of interpretation: (1) a theory

invoking space charge buildup and saturation is proposed to explain the continuously moderated response, rather than fitting straight line segments to the data; and (2) the pressure-independent readings below  $10^{-12}$  Torr are ascribed to leakage current in an out-of-strike state rather than to ion current. The data presented in Fig. 18 represent the response of clean Redhead gauges operated with the recommended potential of 4,800 volts and a magnetic field of 1,040 gauss.

The ultrahigh vacuum portion of the response curve for clean GCA Model 1410 (Kreisman) gauges (Fig. 19) shows the following characteristics: (1) a background leakage current corresponding to an indicated pressure reading of about  $4.5 \times 10^{-14}$  Torr for any real gas pressure value below  $1.7 \times 10^{-10}$  Torr; i.e., for pressures below operating threshold, the gauge remains in the out-of-strike state; (2) a total current value of  $7 \times 10^{-13}$  amp for initiation of a discharge; this threshold level corresponds to an indicated pressure reading of  $3.5 \times 10^{-13}$  Torr and a real pressure of  $1.7 \times 10^{-10}$  Torr; (3) a nonlinear response curve for values above threshold with a continuously moderated slope, due to the self-moderation of space charge buildup; (4) a region of instability around  $10^{-8}$  Torr; and (5) a sensitivity above  $10^{-8}$  Torr which continues to increase with pressure along a response curve of slope 1.11; thus a linear response is not achieved over any portion of the pressure range. This latter feature is also found<sup>19/</sup> for a Redhead flight gauge from which auxiliary cathodes have been removed.

Kreisman reported<sup>18/</sup> the current-pressure characteristics of two standard GCA Model 1410 gauges. The first gauge exhibited linear response over one decade of pressure from  $5 \times 10^{-8}$  to  $5 \times 10^{-7}$  Torr. The second gauge gave a nonlinear response curve (of slope 1.10) for the pressure range from  $6 \times 10^{-9}$  to  $1 \times 10^{-6}$  Torr, no data were given for pressures below the  $10^{-9}$  Torr range. Thus, the data in the range reported<sup>18/</sup> for the second gauge agree with the response curve, Fig. 19, given here.

The threshold phenomenon may be repeatedly observed by raising and lowering the real pressure around the value necessary to sustain a discharge, i.e.,  $2.7 \times 10^{-12}$  Torr for NRC 552 and  $1.7 \times 10^{-10}$  Torr for GCA 1410 gauges. To accomplish small pressure changes around the threshold values, the helium flow rate was slightly increased and decreased by varying the Vycor-helium diffuser temperature. Although the small pressure changes are recorded by the reference ion gauge, large step-wise changes from the background to the threshold value are indicated by the magnetron gauges. In addition, the magnetron gauges do not respond to pressure changes below their threshold pressure levels; i.e., the steady background leakage current values are indicated without an ion current component for all pressures below the threshold level.

Qualitatively, at least, the threshold phenomenon may be thought of in terms of the minimum number of avalanche initiating electrons required for a sustaining discharge. Figure 16 illustrates the process by which electrons may escape from the cathode and enter the trapping region as avalanche initiators. An avalanche initiating electron may make an ionizing collision, for example, with a gas molecule, and lose sufficient energy so that it will travel in an approximately hypercycloidal path which does not intersect the cathode. The secondary electron produced by the ionization normally is also trapped in the discharge. However, for magnetron devices operated below cutoff, as is the case for both gauges discussed herein, electrons emitted from the cathode will execute approximately hypercycloidal paths which intersect the cathode on the first orbit (see Fig. 16) unless a collision occurs, leading to a high probability of recapture. For the electric and magnetic field values employed in these gauges, an avalanche will not develop unless a sufficient number of gas molecules exists inside the anode cage to provide the threshold number of avalanche initiating collisions.

The total cathode current corresponding to threshold for the magnetron gauges is between 7 and  $9 \times 10^{-13}$  amp, including currents from avalanche initiating electrons, ions and background. Since this total value is four to seven times greater than the background alone, there is a clearly distinguishable difference between operation of the gauges above and below threshold. Even the cleanest tubes exhibit this threshold phenomenon.

The real pressure corresponding to threshold is about 60 times different for the two magnetron designs (see Fig. 20), which suggests a possible difference in the number of electrons available for avalanche initiation. Differences between at least two parameters of these gauges lead to a prediction of different electric field values at the cathode surfaces: (1) the recommended operating potential is 800 volts lower for the GCA 1410 gauge; and (2) the central cathode radius is about double that used in the NRC 552 gauge (see Fig. 17). Whether or not these differences alone are sufficient to account for the difference in threshold pressures is an open question.

The continuously modified, nonlinear-response curve above threshold and the approach to linear response due to space charge saturation are two additional qualitative characteristics observed experimentally for both magnetron gauges. However, we again note that quantitative values are different (see Fig. 20) for the two commercial designs. The nonlinear response above the threshold is steeper for the Kreisman tube, beginning with a slope of about 14 and reaching 1.11, whereas the Red' ad response curve begins with 2.2 and reaches a nearly linear slope of 1.04. These differences may be viewed alternatively in terms of an increase with pressure of the ionization probability or the number of ionizing electrons in the contained discharge.

The containment of space charge appears to be relevant to the attainment of linear response. The unique feature of auxiliary cathodes in the Redhead design permits a much closer spacing between cathode and anode electrodes; thus, the anode cage is tightly enclosed electrostatically and the space charge is apparently contained within this fixed volume at a more closely saturated value. It is interesting to note, in closing, that calibration of the flight model NRC magnetron design,<sup>19/</sup> in which no auxiliary cathodes are used gave a response curve with a slope of 1.15. That is, the flight model magnetron response was similar to the 1.11 slope of the Kreisman design for normal operation above  $10^{-10}$  Torr. Thus the data for flight gauges<sup>19/</sup> and Kreisman gauges both without auxiliary cathodes show only an approach to saturation and linearity. On the other hand, the response (1.04 slope) of regular Redhead gauges with auxiliary cathodes and the electrostatically tight anode cage which results, exhibits almost complete fulfillment of the space charge saturation hypothesis for linear response, which is described in this report.

The Redhead and Kreisman gauge designs may be described as magnetrons operated below cutoff since electrons may not energetically travel from cathode to anode without g. molecule interactions. A residual electron current across the electrode gap is forbidden in these designs by the electrode and magnet field arrangements.

The trigger discharge gauge arrangement does not absolutely exclude electron flow from cathode to anode. Electrons may travel parallel to the magnetic field from the cathode plates to the edge of the anode cylinder, a distance of 0.8 mm. Earlier Penning cell designs were limited by such a residual current background; however, the trigger discharge gauge appears to be operating at the threshold for such residual current. The individual condition and history of a gauge tube can significantly affect the residual current. Thus the operation of a magnetron gauge generally yields a recognizable drop at the low pressure end, as seen in Figs. 18, 19, and 20, corresponding to a loss of ion current. Whereas, trigger gauge operation is often confused by residual current as seen in Fig. 21.

Two general cases exist for the trigger discharge gauge response below  $10^{-9}$  Torr. In the first case the tube loses the ion current component near  $10^{-10}$  Torr and drops to a background current of about  $10^{-13}$  amp (see Fig. 22). The second case in which ion current is maintained for gas pressures below  $10^{-10}$  Torr is characterized by the presence of some spurious current, Figs. 21 and 22. Ion current is present whenever the discharge exists as should be expected. In the second case another source of current becomes significant. This source is in addition to the leakage current background. The probable sources for this erroneous current are electron field emission from cathode to anode and secondary electron emission from the cathode under ion bombardment.

Figures 21 and 22 show the variations which may occur in the trigger discharge gauge response. No single response curve is followed for pressures below  $10^{-8}$  Torr. Figure 23 gives a response curve for pressures above  $10^{-8}$  Torr showing a nonlinear increase of ion current with pressure until a glow type discharge and ion recombinations limit response near  $10^{-4}$  Torr.

### C. A Field Emission Microscope Study

A new field emission microscope tube was constructed in which the emitter tip can be cooled without significant cooling of the inner wall of the microscope tube (see Fig. 24). This feature permits cryosorption of atoms onto the tip from a gas without significantly altering the equilibrium pressure of that gas. Therefore, the number density of atoms can be studied without significantly influencing the total number. The geometry of this new microscope tube has been arranged so that a line of sight path is possible for gas molecules between each of the following three units: a nude modulated Bayard-Alpert type ionization gauge, a nude source partial pressure analyzer, and the microscope tip. That is, the three units are arranged in a line of sight within high conductance tubulation, so that they may all detect the same equilibrium gas pressure.

The field emission microscope technique has been employed to observe gas dynamics<sup>1/</sup> in a form which may represent individual atomic locations. Although the resolution of the microscope is not sufficient to determine atomic sizes it should be possible to observe the enhanced emission from an atomic size spot on the emitter tip.

Time lapse data have shown an order of magnitude agreement between the rate of arrival of new spot images and the abundance of atomic species which could cause such an enhanced emission. Several uncertainties exist, e.g., the partial pressure analyzer indicates that the active species exist in the adsorbed state for the experimental conditions employed. Therefore, it is possible that the process observed should be attributed to migration of gas species in the adsorbed state rather than a gas dynamics process.

The comparison between the field emission microscope technique and partial pressure analyzer data is interesting although it shows the need for more work to verify the data obtained. The partial pressure analyzer should give a nearly linear response in the ultrahigh vacuum range in which the data were obtained. However, the analyzer is not a pressure standard and a favorable comparison with the field emission microscope data is not sufficient to justify the latter technique as a standardization method. The next step in the development of the field emission microscope method for gas pressure measurement is to compare it with a recognized standard for pressure determinations.

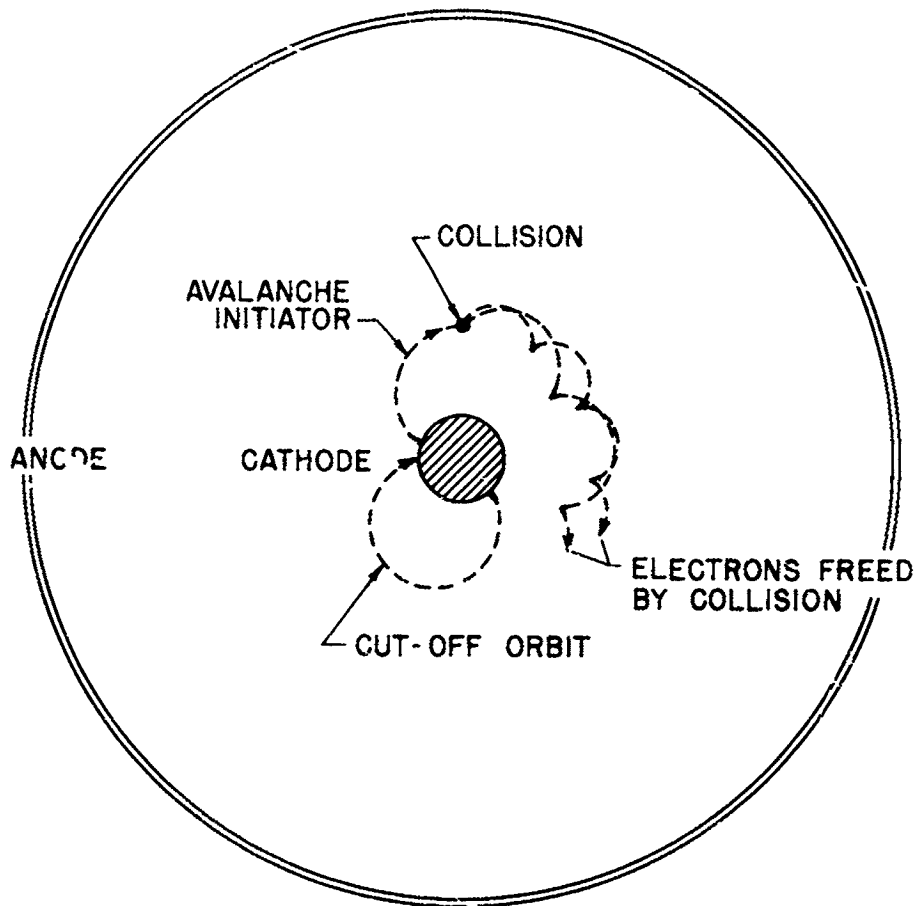


Fig. 16 - Electron Orbits in a Coaxial Magnetron Structure. Electrons either return to the cathode or collide with gas molecules to change their momentum and in event of ionizing collisions to release secondary electrons.

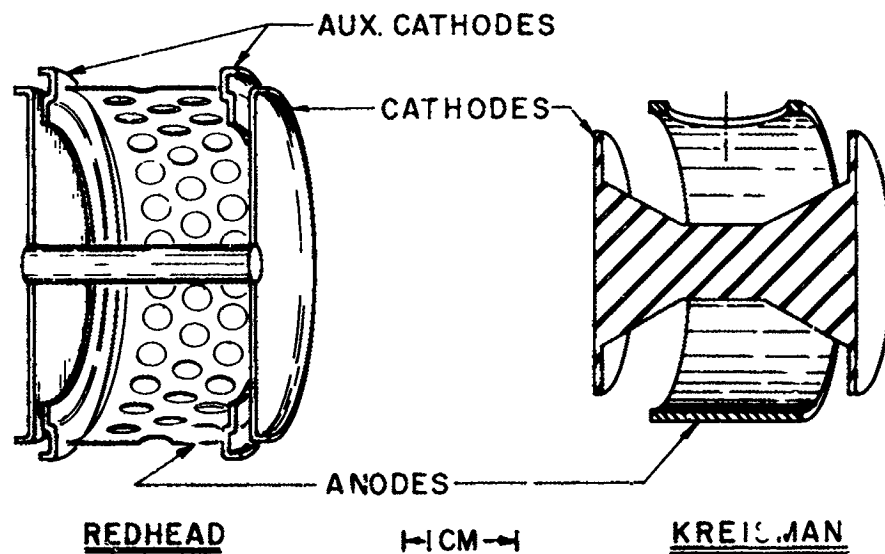


Fig. 17 - Electrode Configurations of Commercial Magnetron Gauges, Shown to Scale in Cutaway; Anode Diameters: Redhead 3.0 cm., Kreisman 2.5 cm.

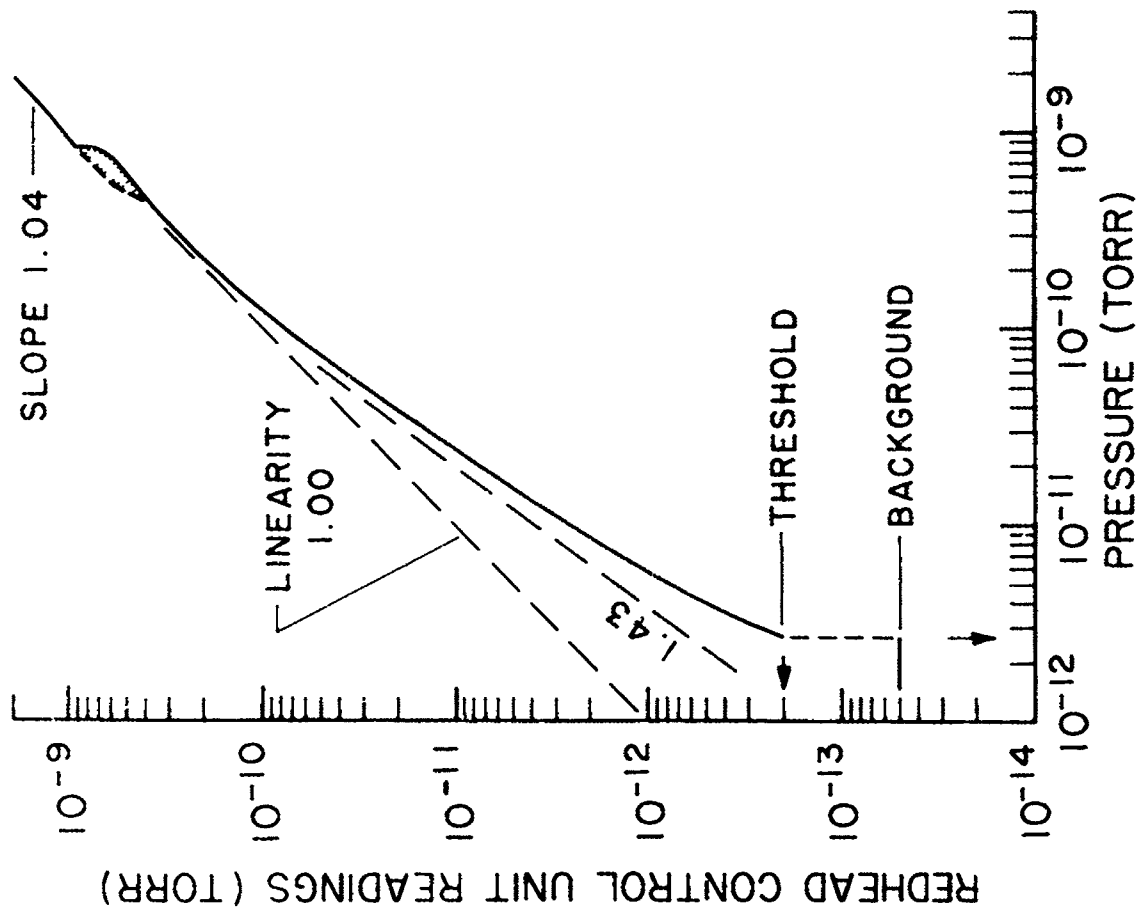


Fig. 18 - Characteristic Response of Clean Redhead (NRC 552 glass envelope) Gauges. Ultrahigh vacuum range shows: background reading below threshold; sensitivity rise with pressure; and unstable region around  $7 \times 10^{-10}$  Torr; and near linear response above that region.

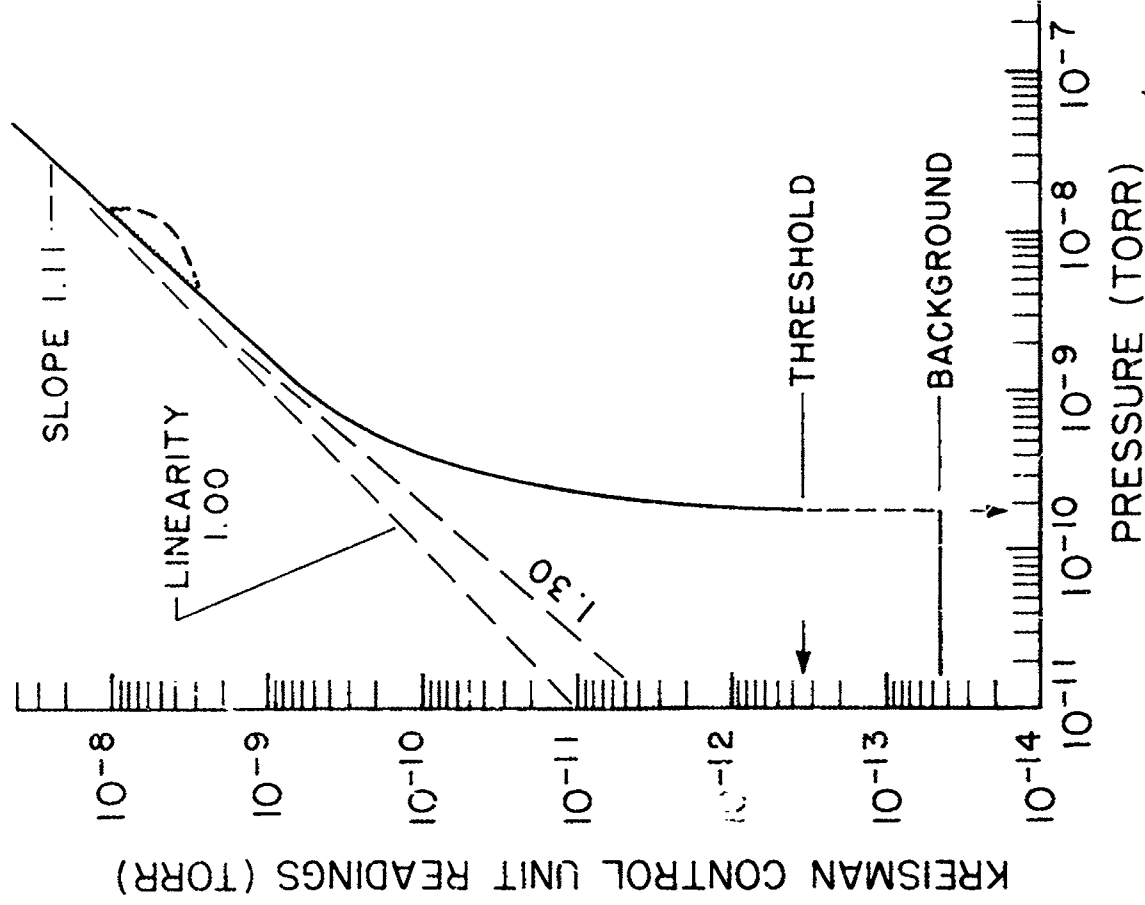


Fig. 19 - Characteristic Response of Clean Kreisman (GCA 1410) Gauges, Showing: Background Indicating  $10^{-14}$  Torr Range for Pressures Below Threshold of  $1.7 \times 10^{-10}$  Torr; a Rapid Buildup; a Possible Unstable Region Near  $10^{-8}$  Torr; Followed By a Steady Sensitivity Rise Along a 1.11 Slope.

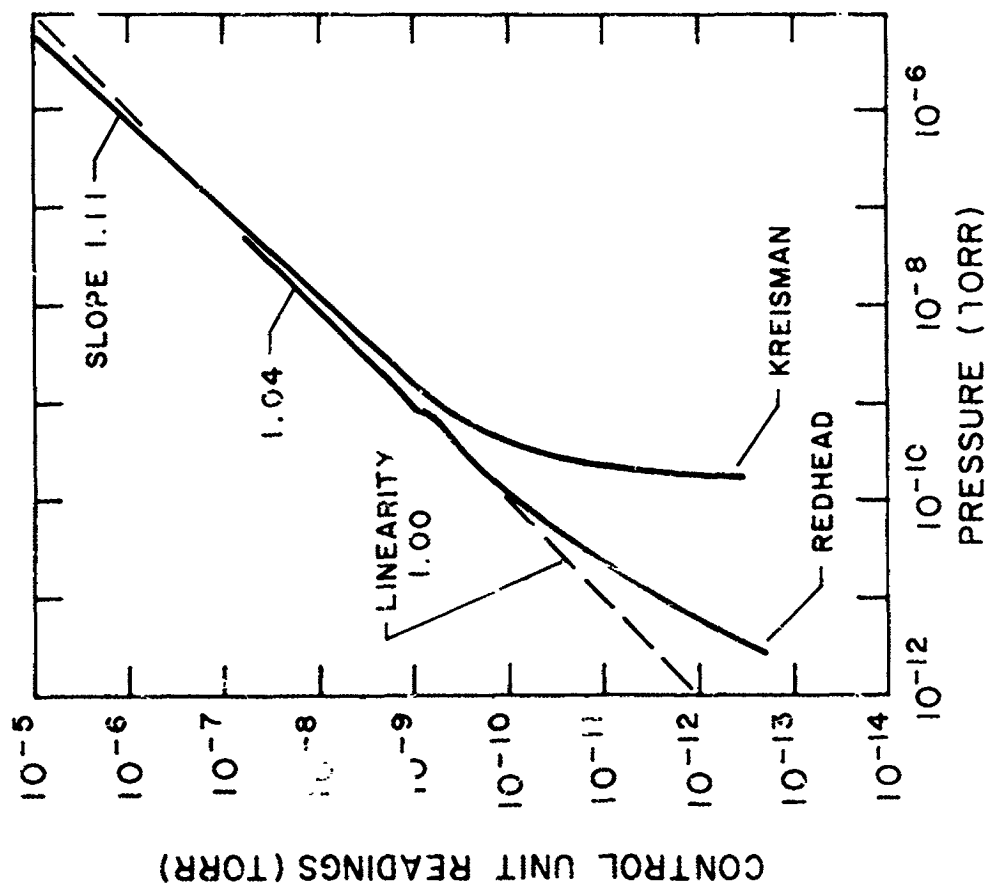


Fig. 2C - Characteristic Response Curves for Two Magnetron Gauge Models (upper portion of Redhead curve omitted) Showing Differences Which Result from Variations in the Designs

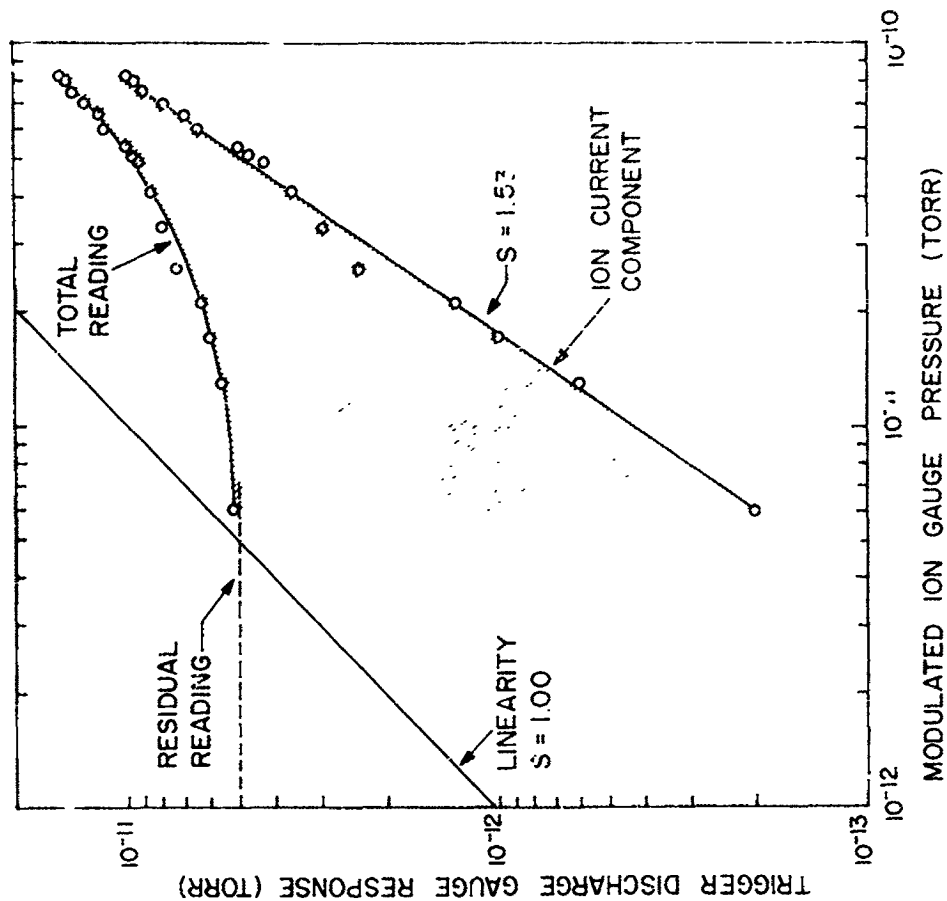


Fig. 21 - An Example of Trigger Discharge Gauge, TDG, (GE Model 22 GT 214) Response Showing an Asymptotic Approach to a Residual Reading Which Distorts the Ion Current Response. Correction for the apparent background reading gives an estimate of ion current; other TDG tests may vary as indicated in Fig. 22.

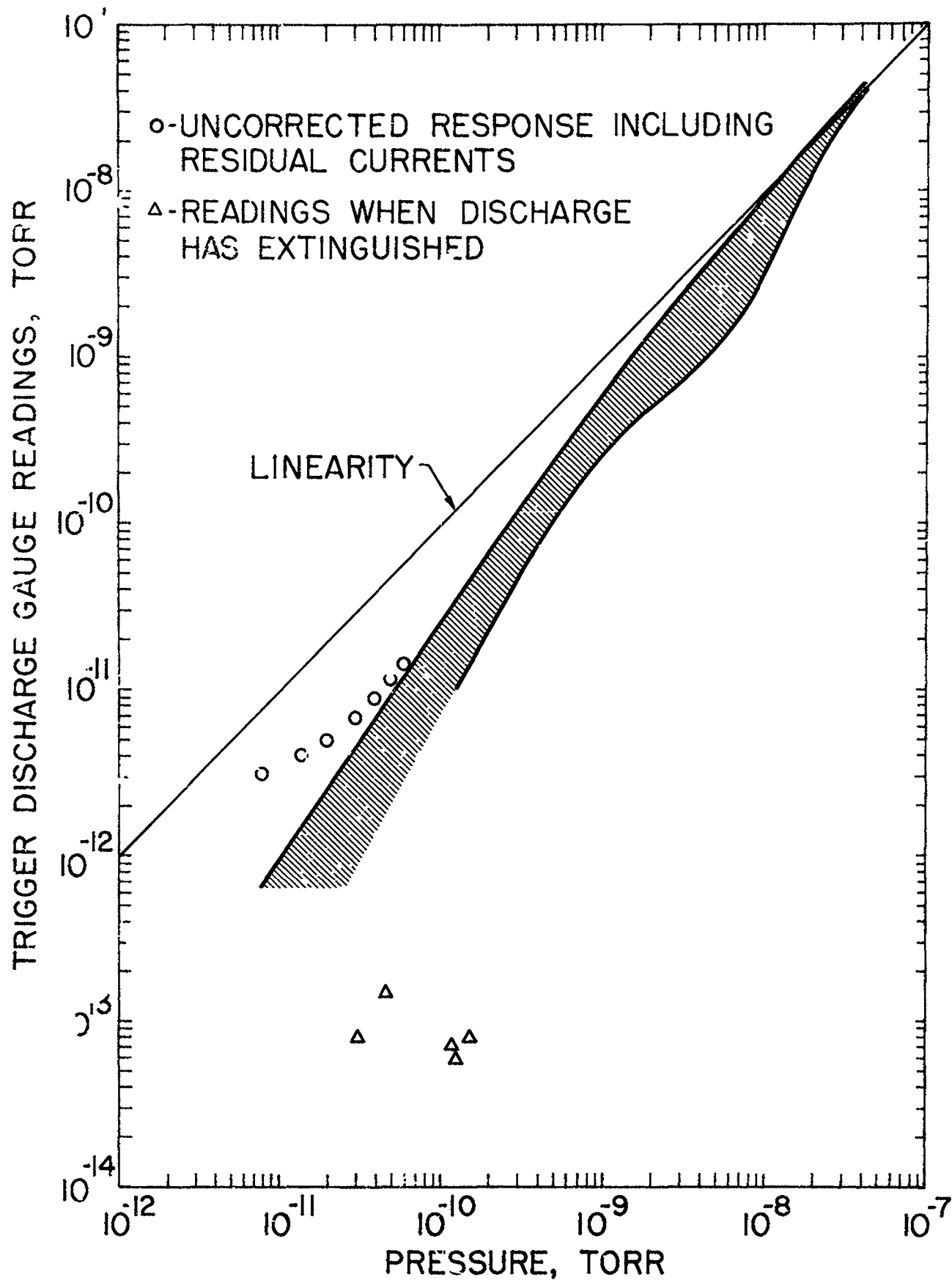


Fig. 22 - TDC Response for the UHV Range; the Ion Current Component Lies within the Shaded Region; Residual or Background Currents Can Give Higher Total Readings, e.g., see Circular Data Points; Loss of the Discharge and Ion Current May Give Lower Readings, e.g., see Triangular Data Points

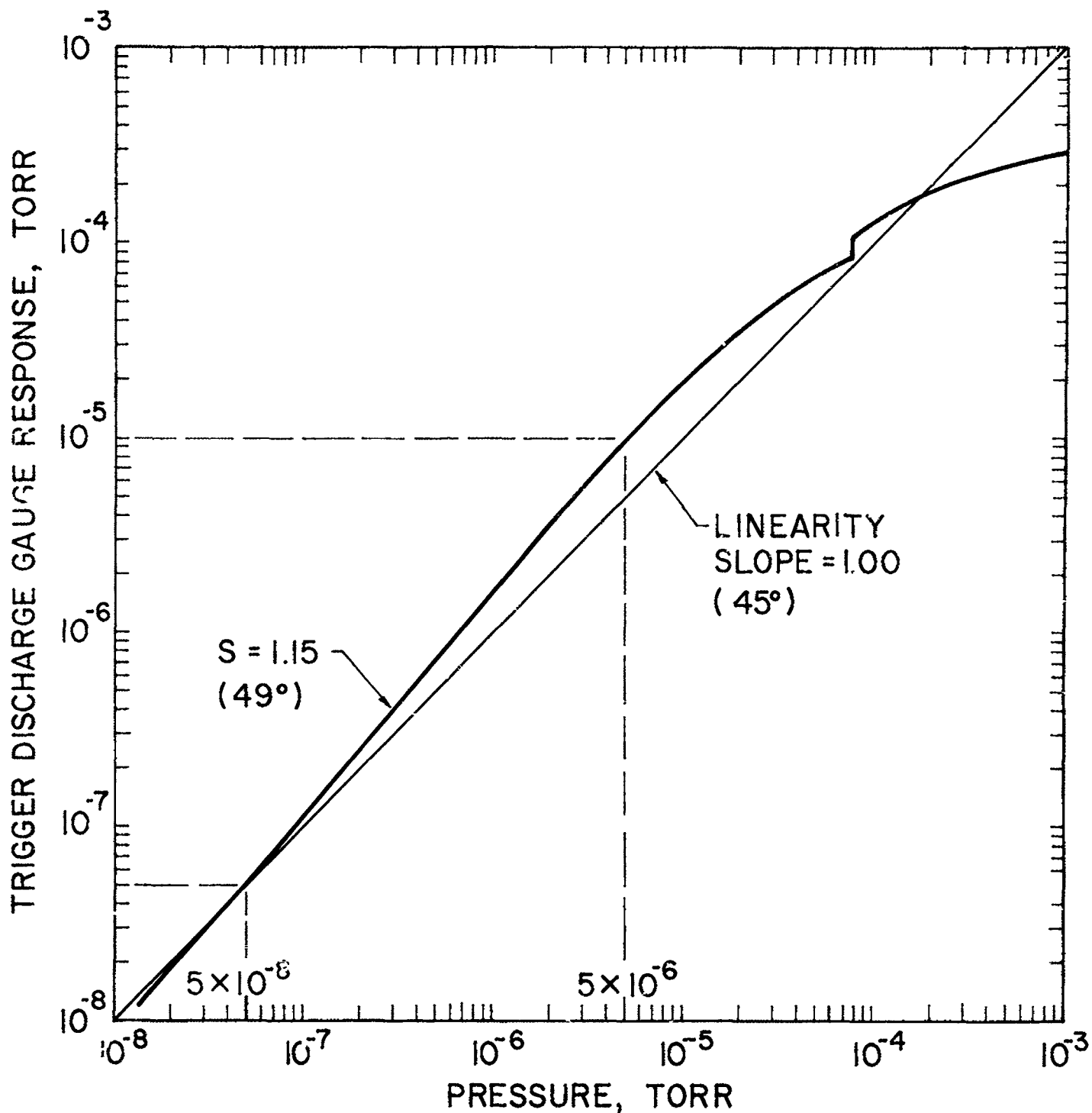


Fig. 23 - TDG Response above 10<sup>-8</sup> Torr Giving Direct Readings from Gauge Control Unit with 2.5 Amp/Torr Sensitivity. The nonlinear TDG readings reach a factor of two greater than linear response around 5 × 10<sup>-6</sup> Torr, then approach saturation above 10<sup>-4</sup> Torr.

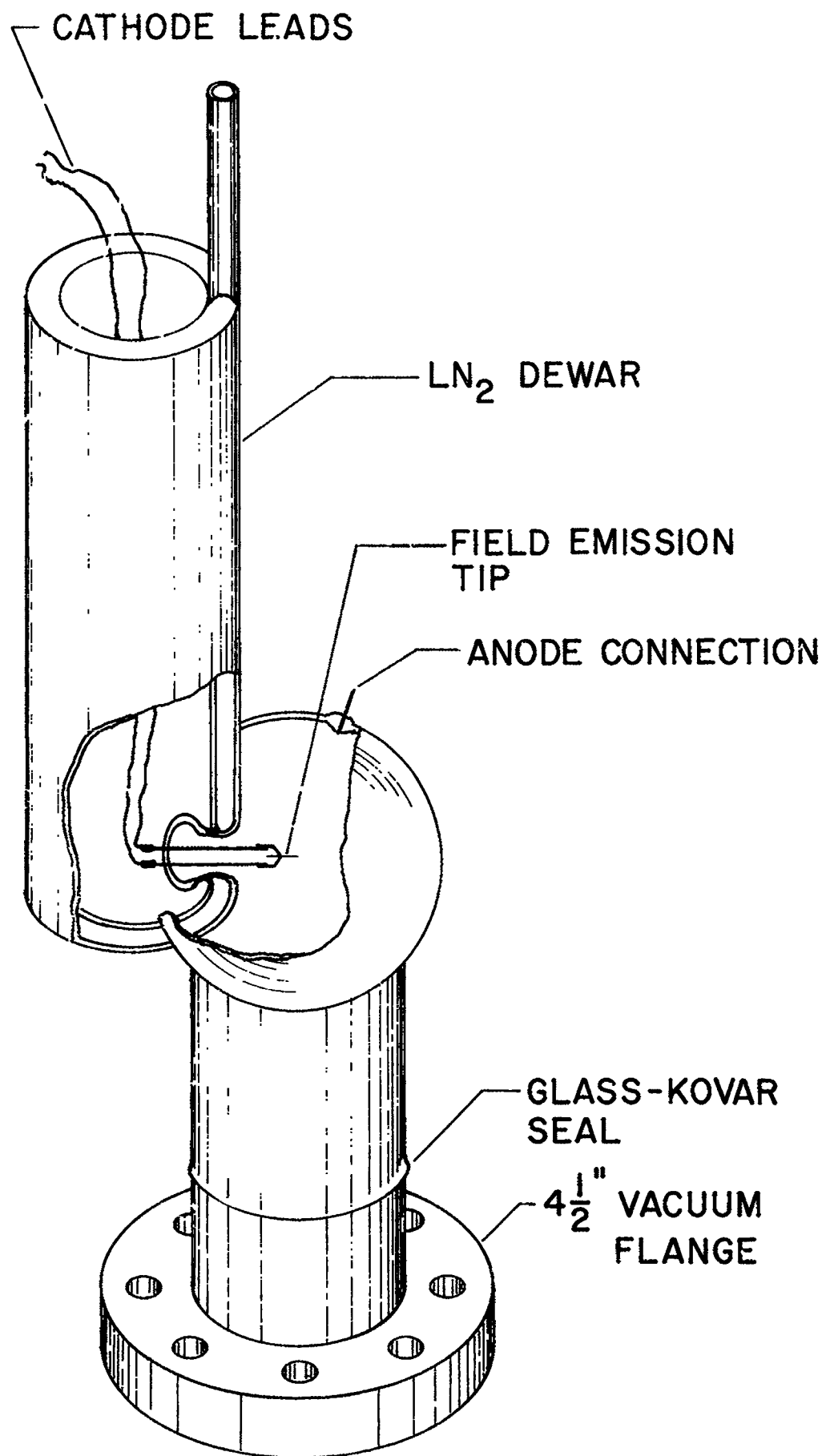


Fig. 24 - Electron Field Emission Microscope Tube for Gas Dynamics Study; Metal Tip May Be Selectively Cooled without Significantly Cooling Inner Wall or Changing Equilibrium Gas Pressure

#### IV. DISSEMINATION OF INFORMATION DEALING WITH VACUUM SCIENCE

The nature of the work performed on Contract NASr-63(06) is such that it has widespread application in the many fields using vacuum technology. Therefore, the data, interpretations, and conclusion obtained from this program have been made available not only by publications<sup>26,27,28/</sup> but also by seminar presentations at each of the six NASA branch facilities and by technical consultation on special problems with the personnel from the branch laboratories.

A. Seminar programs were presented at the NASA branch laboratories: Manned Spacecraft Center, Langley Research Center, Lewis Research Center, Ames Research Center, Goddard Space Flight Center, and the Marshall Space Flight Center. The programs dealt primarily with the topics:

1. Pressure measurements in UHV systems,
2. Partial Pressure Analysis of UHV systems,
3. Cold welding and clean surface studies,
4. Operational characteristics of vapor pumps,
5. Field emission microscopy and adsorption,
6. Cryopanel characteristics, and
7. Special Applications of UHV Techniques.

B. Consultation on special problems was conducted not only while visiting the various branch facilities but also by telephone and at MRI. Calibration curves for gauges and systems were determined as part of this service.

In conclusion, this seminar and consultation phase of the work have proven to be effective for information dissemination and have provided a quick response to localized problems at the various NASA branch facilities.

## REFERENCES

1. Bryant, P. J., C. M. Gosselin, and W. W. Longley, Jr., NASA CR-324 (1965).
2. Taylor, L. H., W. W. Longley, Jr., and P. J. Bryant, Journal of Chemical Physics, 43, 1184-1189 (1965).
3. Simpson, P. A. and A. H. Morgan, NBS Report 6080, Oct. 1959 (NBS Project 8420-12-8922).
4. Hirschfelder, J. O., C. F. Bird, and R. B. Bird, Molecular Theory of Gases and Liquids (John Wiley & Sons, Inc., New York, 1954).
5. Halsey, Jr., G. D., Trans. Natl. Vac. Symp., 1961, 119 (1962).
5. Bryant, P. J., C. M. Gosselin, and L. H. Taylor, NASA CR-84 (1964).
7. Florescu, N. A., Australian J. Appl. Sci., 8, 305 (1957).
8. Penning, F. M., Physics, 3, 873 (1936).
9. Young, J. R., and F. P. Hession, Trans. Natl. Vac. Symp., 9th, 234 (Macmillan, 1963).
10. Beck, A. H., and A. D. Brisbane, Vacuum, 2, 137 (1952).
11. Haefer, R., Acta Physica Austriaca, 7, 52 and 251 (1953); 8, 213 (1954).
12. Redhead, P. A., Can. J. Phys., 36, 255 (1958).
13. Hobson, J. P., and P. A. Redhead, Can. J. Phys., 36, 271 (1958).
14. Redhead, P. A., Can. J. Phys., 37, 1260 (1959).
15. Hobson, J. P., Can. J. Phys., 37, 300 (1959).
16. Kreisman, W. S., and R. Herzog, GCA Technical Report 61-18-N (1961).
17. Kreisman, W. S., GCA Technical Report No. 64-8-N (1964).
18. Kreisman, W. S., GCA Technical Report No. 64-17-N (1964).
19. Newton, G. P., D. T. Pelz, G. E. Miller and R. Horowitz, Trans. Natl. Vac. Symp., 10th, 208 (Macmillan, 1963).

20. Rutherford, S. L., Trans. Natl. Vac. Symp., 9th, 185 (Macmillan, 1963).
21. Jepsen, R. L., J. Appl. Phys., 32, 2619 (1961).
22. Redhead, P. A., Can. J. Phys., 43, 1001 (1965).
23. Roehrig, J. R., and J. C. Simons, Jr., Trans. Natl. Vac. Symp., 8th, 511 (Pergamon Press, 1962).
24. Redhead, P. A., Rev. Sci. Instr., 31, 343 (1960).
25. Feakes, F., and F. L. Torney, Jr., Trans. Natl. Vac. Symp., 10th, 257 (Macmillan, 1963).
26. Gosselin, Charles M., and Paul J. Bryant, J. Vac. Sci. and Tech., 2, no. 6, 293-297. Nov./ Dec. 1965 (See appendix).
27. Taylor, Lyle H., William W. Longley, Jr. and Paul J. Bryant, J. Chem. Phys., 43, No. 4, 1184-1189, 15 August 1965 (See appendix).
28. Bryant, Paul J., William W. Longley, Jr., and Charles M. Gosselin, J. Vac. Sci. and Tech., 3, No. 2 March/ April 1966.

## APPENDIX

# Residual-Gas Analysis of a DC-705 Oil-Diffusion-Pumped uhv System\*

Charles M. Gosselin and Paul J. Bryant

Midwest Research Institute, Kansas City, Missouri

(Received 14 June 1965)

The residual gases present in a DC-705 oil-diffusion-pump uhv system have been determined as a function of various trapping conditions. The system was equipped with a metal 2-in. oil-diffusion pump in series with a specially designed trap in which zeolite was used. The configuration of the trap permitted the trapping zone to be immersed in cryogenic liquids, e.g., LN<sub>2</sub>. The effectiveness of the trap was determined as a function of temperature. A comparison of the residual gases is made for six conditions, including three trapping temperatures, while operating with zeolite and without zeolite.

## Introduction

Diffusion pumps have long been used to achieve high-vacuum environments and in recent years uhv environments. The major advantages in using diffusion pumps are their capability to handle large gas loads for extended periods of time and to maintain pumping speed at reduced pressures. The limitations associated with the diffusion-pumping technique are often established by the fluid used as a pumping media and the trapping technique used to isolate this fluid from the uhv chamber. Pressures well into the uhv range have been achieved using both mercury<sup>1,2</sup> and oil<sup>3</sup> as a pumping fluid in conjunction with optically dense liquid-nitrogen baffles. Oil has also been used successfully with optically dense traps which contain zeolite or activated alumina at room temperature to obtain uhv pressures.<sup>4</sup> However, in addition to obtaining a low total pressure, it is important to know the type and quantities of residual gases within an uhv chamber due to the pumping fluid and trapping combination.

A study of the residual gases present in an uhv system for various trapping conditions was conducted to determine the contamination resulting from the use of DC-705 pumping fluid.

## 1. Equipment

The apparatus used in this study can be divided into three major components, i.e., the partial-pressure analyzer system (PPAS), the experimental trap, and the

oil-diffusion-pump system.

1. The PPAS (shown in Fig. 1) consists of a G.E. model 514 partial-pressure analyzer (PPA), an 8-liter/sec getter-ion pump, two closed-grid ionization gauges, and the associated plumbing.

The analyzer unit (first described by Davis and Vanderslice<sup>5</sup> and later by Davis<sup>6</sup>) is a magnetic focusing device using a 5-cm radius of curvature and a 90° sector. It is equipped with a Nier-type ionization source and a ten-stage electron-multiplier ion detector. A variable field strength electromagnet (0 to 6.5 KG) is used with the PPA. Magnetic-sweeping techniques are, therefore, employed in the collection of data.

An 8-liter/sec getter-ion pump is connected to the analyzer system to provide an environment in which

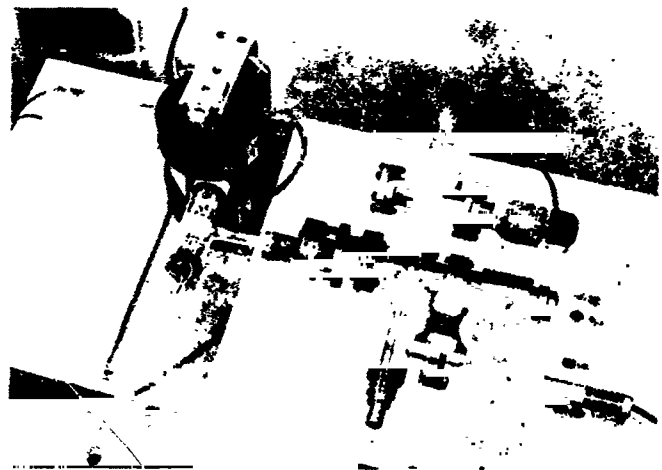


FIGURE 1. Partial-pressure analyzer system (PPAS). Consists of a G.E. model 514 analyzer (PPA) with a 6.5 KG electromagnet, an 8-liter/sec getter-ion pump, ionization gauges, and appropriate plumbing.

\* This work was supported by the National Aeronautics and Space Administration, Headquarters, Washington, D. C., under contract NASr-63(06).

<sup>1</sup> A. Venema, *Vacuum* 9, No. 1, 54-57 (1959).

<sup>2</sup> P. J. Bryant and C. M. Gosselin, *1961 Transactions of the Eighth National Vacuum Symposium and Second International Congress* (Pergamon Press, Inc., New York, 1962), pp. 1224-1227.

<sup>3</sup> M. H. Hablanian and P. L. Vitkus, *1963 Transactions of the Tenth National Vacuum Symposium* (The Macmillan Company, New York, 1963), pp. 140-146.

<sup>4</sup> M. A. Biondi, *1960 Transactions of the Seventh National Vacuum Symposium* (Pergamon Press, Inc., New York, 1961), pp. 24-28.

<sup>5</sup> W. Davis and T. Vanderslice, *1960 Transactions of the Seventh National Vacuum Symposium* (Pergamon Press, Inc., New York, 1961), pp. 417-420.

<sup>6</sup> W. D. Davis, *1962 Transactions of the Ninth National Vacuum Symposium* (The Macmillan Company, New York, 1963), pp. 363-370.

the PPA is maintained clean and in operating condition between data-collection periods. A 1½-in. isolation valve is installed between the analyzer and the getter-ion pump so that the effects of the active surfaces of the getter-ion pump may be eliminated during the analysis of a test system.

Total pressure measurements are obtained by one of two glass ionization gauges. The other gauge is operated under a variety of electrical conditions to aid in determining the effects of ionization gauges on the residual gas spectra.

The remainder of the PPAS is constructed of 304 stainless steel and Kovar. Since all of the flange seals are made with copper gaskets, the entire PPAS (less electronic connection and magnet) is bakeable to 400°C.

2. The experimental trap (shown in Fig. 2) is constructed of 304 stainless steel and is similar in design to the chemical trap proposed by Biondi.<sup>4</sup> The trap is all heli-arc welded, and thus fully bakeable. The design of the chemical zone or sump is such that it can be submerged in cryogenic fluids, e.g., liquid nitrogen or a dry ice and acetone slurry. Zeolite (CVC Absorbant-A) is placed in the base of the sump and in the annular tray at the lower end of the vertical tube. This configuration is not only optically dense but also eliminates oil-creep paths along walls of the trap (to the effective limit of the zeolite).

3. The oil-diffusion-pump system (shown in Fig. 3) consists of a 2-in. pump backed by a 1-in. booster pump, a foreline valve, chemical foreline trap and a mechanical forepump. The 2-in. pump is trapped by a water-cooled chevron baffle. Gold O-ring seals are used between the 2-in. pump and baffle.

Copper-gasket seals were used to connect the diffusion-pump system, the experimental trap, and the

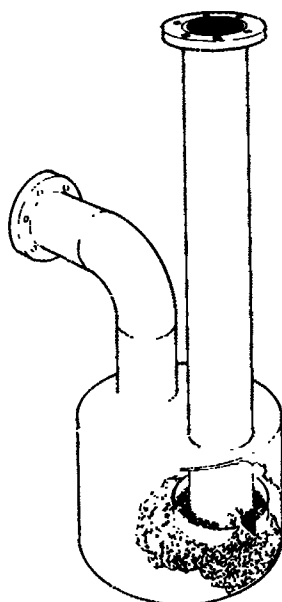


FIGURE 2. Special chemical trap in which the trapping zone can be submerged into cryogenic fluids. Trap is constructed of heli-arc welded 304 stainless steel. Zeolite is placed in lower part of sump and in annular tray at base of vertical tube.

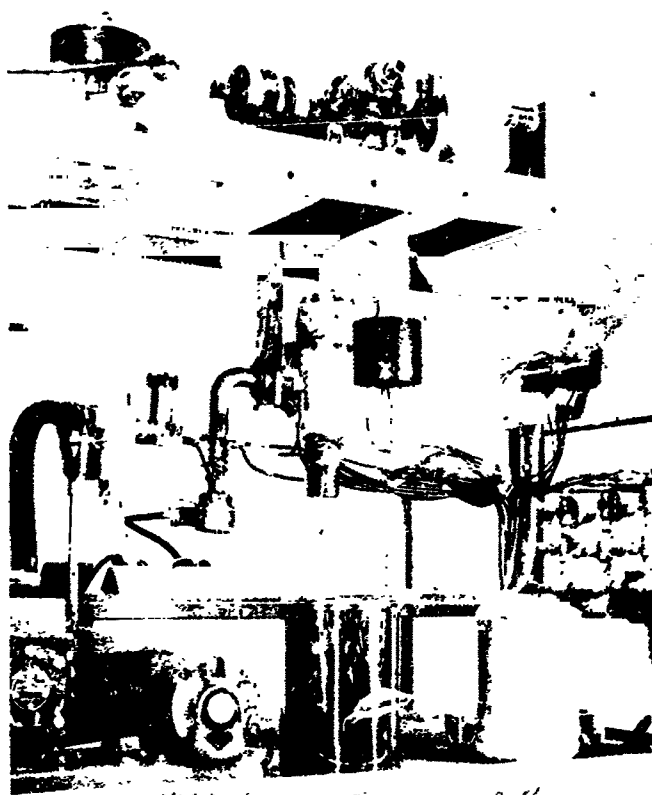


FIGURE 3. Oil-diffusion-pump system and chemical trap mounted immediately below the PPAS and attached by means of a 1½-in. valve. Dewar and heating mantle for chemical trap are shown.

PPAS. Therefore, the bakeable portion of the system extends from the top of the 2-in. diffusion pump to and including the PPAS.

When using the above described system, a three-step bakeout procedure is required. (a) Following an initial pump-down from air, the PPAS is isolated by closing the 1½-in. valve to the zeolite trap. The trap and uhv line to chevron baffle are then baked to 400°C. (b) After cooling the trap to room temperature and reopening the isolation valve, the PPAS is baked at 400°C. Approximately 1h before cooling the analyzer system, the trap is submerged into a bath of LN<sub>2</sub>. (c) After cooling and again isolating the PPAS, the trap and uhv line to chevron baffle is rebaked.

## II. Results

A summary of the data collected is presented in Table I. The columns list the Torr-air equivalent pressure for each gas species found in the system during the various conditions. The partial-pressure measurements were obtained by determining the percentage of the total ion current detected by the PPA for particular gas species and by applying these percentages to the total-pressure ionization-gauge reading. The gauge control used in this study was calibrated for dry air. Therefore, pressures are reported in Torr-air equivalent units. No gauge factors (correction for ionization efficiencies) for the various gases have been used.

TABLE I. Residual gases in an oil-diffusion-pumped uhv system for several trapping conditions (pressure reported in Torr-air equivalent units)

Gas	Background	Zeolite in trap			No zeolite in trap		
		-196°C	-78°C	25°C	-196°C	-78°C	25°C
H <sub>2</sub>	$1.3 \times 10^{-10}$	$2.1 \times 10^{-9}$	$2.1 \times 10^{-9}$	$1.8 \times 10^{-9}$	$3.1 \times 10^{-9}$	$2.5 \times 10^{-9}$	$2.2 \times 10^{-9}$
He	$5.1 \times 10^{-11}$	...	...	...	...	...	...
CH <sub>4</sub>	$2.2 \times 10^{-10}$	$1.7 \times 10^{-11}$	$6.8 \times 10^{-11}$	$7.1 \times 10^{-11}$	$1.6 \times 10^{-11}$	$8.3 \times 10^{-11}$	$1.3 \times 10^{-10}$
H <sub>2</sub> O	$1.6 \times 10^{-12}$	$8.4 \times 10^{-12}$	$8.7 \times 10^{-12}$	$7.3 \times 10^{-12}$	$9.4 \times 10^{-12}$	$5.0 \times 10^{-12}$	$6.3 \times 10^{-12}$
C <sub>2</sub> H <sub>2</sub>	...	...	...	...	...	...	$1.3 \times 10^{-12}$
C <sub>2</sub> H <sub>4</sub>	$5.0 \times 10^{-12}$	$1.1 \times 10^{-12}$	$4.8 \times 10^{-12}$	$3.3 \times 10^{-11}$	$6.1 \times 10^{-12}$	$8.8 \times 10^{-11}$	$1.2 \times 10^{-10}$
CO	$7.8 \times 10^{-11}$	$1.5 \times 10^{-11}$	$2.1 \times 10^{-11}$	$5.7 \times 10^{-11}$	$2.1 \times 10^{-11}$	$1.3 \times 10^{-10}$	$2.0 \times 10^{-10}$
C <sub>2</sub> H <sub>6</sub>	$3.4 \times 10^{-12}$	$1.3 \times 10^{-12}$	$8.2 \times 10^{-12}$	$9.5 \times 10^{-12}$	$1.2 \times 10^{-12}$	$7.8 \times 10^{-12}$	$1.9 \times 10^{-11}$
Ar	$5.8 \times 10^{-13}$	...	...	...	...	...	...
C <sub>3</sub> H <sub>8</sub>	...	$6.3 \times 10^{-13}$	$7.2 \times 10^{-13}$	$2.1 \times 10^{-12}$	$4.7 \times 10^{-13}$	$2.2 \times 10^{-12}$	$4.6 \times 10^{-12}$
CO <sub>2</sub>	$2.6 \times 10^{-12}$	$2.1 \times 10^{-12}$	$2.4 \times 10^{-12}$	$3.6 \times 10^{-12}$	$2.6 \times 10^{-12}$	$3.8 \times 10^{-12}$	$4.7 \times 10^{-12}$
C <sub>4</sub> H <sub>8</sub>	...	...	...	...	$3.6 \times 10^{-13}$	$8.3 \times 10^{-13}$	$2.0 \times 10^{-12}$
C <sub>4</sub> H <sub>6</sub>	...	$8.4 \times 10^{-14}$	$1.8 \times 10^{-13}$	$1.1 \times 10^{-10}$	$6.4 \times 10^{-13}$	$6.3 \times 10^{-10}$	$5.3 \times 10^{-10}$
C <sub>7</sub> H <sub>8</sub>	...	...	...	...	...	...	$2.3 \times 10^{-12}$
C <sub>8</sub> H <sub>10</sub>	...	...	...	...	...	$3.0 \times 10^{-12}$	$9.1 \times 10^{-13}$
Total	$4.8 \times 10^{-10}$	$2.1 \times 10^{-9}$	$2.2 \times 10^{-9}$	$2.1 \times 10^{-9}$	$3.2 \times 10^{-9}$	$3.8 \times 10^{-9}$	$3.3 \times 10^{-9}$

The background spectrum (first column of data in Table I) was recorded when only the PPA and one of the ion gauges were operating. That is, the analyzer had been sealed off from the diffusion pump, the chemical trap and the getter-ion pump by closing the two isolation valves. The pressure remained at  $\sim 5 \times 10^{-10}$  Torr for several days under these conditions.

The gas species which constituted the major portion of the background pressure were hydrogen and methane. It is interesting to note that a significant decrease in methane occurred when either the diffusion pump or the getter-ion pump action was introduced. Following the evaluation of the chemical trap, a preliminary study was undertaken to determine the origin of methane in the PPAS. The results are reported at the end of this section.

The background spectra also indicate reasonably large amounts of carbon monoxide and helium. It has been observed in our work and elsewhere<sup>5, 7, 8</sup> that carbon monoxide is commonly found when hot tungsten-filament devices are used. Helium is present due to permeation from the atmosphere through the warm glass envelope of the ion gauge. Because helium is not pumped well by the ion gauge, the partial pressure of this gas gradually increases with time. When either the getter-ion pump or diffusion pump is operating on the PPAS, no detectable amount of helium is observed. The remainder of the background spectrum indicates relatively small amounts of water, ethene, ethane, argon, and carbon dioxide. Note that no argon is detectable when the system is opened to the diffusion pump.

The diffusion-pump data (getter-ion pump is isolated from system) are displayed in Table I under

two major groups, i.e., "zeolite in trap" and "no zeolite in trap." Each group is divided into three sections corresponding to the trap operating conditions, i.e., submerged in liquid nitrogen or a dry ice and acetone slurry, or at ambient laboratory temperature.

Scanning of the diffusion-pump data indicates that the major gas species in all cases is hydrogen. The relatively large amounts of hydrogen are due to desorption from metal parts in the diffusion pump and chevron baffle which were not baked at high temperature. The absence of helium and argon is explained above.

The objective of this study was to determine the level of contamination in an oil-diffusion-pumped uhv system and to explore methods which would be practical and effective in further reducing the problem of oil contamination. Therefore, it is necessary to establish a criterion for determining contaminating effects.

A review of the hydrocarbon gas species in Table I clearly indicates that benzene (C<sub>6</sub>H<sub>6</sub>) is the species which shows the greatest dependence upon trap temperature. This is not an unexpected observation,<sup>9, 10</sup> since the chemical composition of DC-705 is pentaphenyltrimethyltrisiloxane.<sup>10</sup> The generation of phenyl groups would be expected, due to cracking of the fluid in the boiler of the diffusion pump. The additional hydrogen needed to form benzene would then be available to the phenyl groups during their interactions with the metal wall of the system. The heavier hydrocarbons were determined to be methylated benzenes.

It is also interesting to observe that if significant numbers of parent oil molecules are present in an analyzer, detectable amounts of methyl and phenyl ions would be generated by the ionization source.

<sup>9</sup> J. Hengevooss and W. K. Huber, *Vacuum* 13, No. 1 (1963).

<sup>10</sup> D. J. Cravley, E. D. Tolmie, and A. R. Huntress, *1968 Transactions of the Ninth National Vacuum Symposium* (The Macmillan Company, New York, 1963), pp. 399-403.

<sup>7</sup> D. Lichtman, *J. Vac. Sci. Technol.* 2, 70-74 (1965).

<sup>8</sup> W. J. Lange, *J. Vac. Sci. Technol.* 2, 74-79 (1965).

However, in this investigation, no detectable amounts of methyl or phenyl ions were observed, except for those which appear in the fragmentation patterns for the hydrocarbons found in the system. Therefore, it is concluded that the partial pressure of the parent molecule is very small.

Based on the above references and the data collected in this study, it will be assumed that the amount of benzene (gas) in the system is most representative of the presence of oil contamination in the pressure range  $<10^{-8}$  Torr.

Based on the above assumption, it is interesting to examine the relative changes in the amount of benzene present for the various trapping conditions. (Conditions are established for approximately 5h before data are taken.) The best operating condition is observed for the trap with zeolite at liquid-nitrogen temperature. The presence of the chemical reduces the contamination by a factor of  $\sim 8$  in comparison to the nonzeolite situation. However, the most outstanding effect is noted for the  $-73^{\circ}\text{C}$  condition. At this temperature, the zeolite is responsible for reducing contamination by a factor of  $\sim 350$ . Note also that the difference between the  $-78^{\circ}\text{C}$  zeolite condition and the  $-196^{\circ}\text{C}$  nonzeolite condition is only a factor of  $\sim 3$ . The reduction of benzene due to the chemical for ambient laboratory temperature is by a factor of  $\sim 5$ . Ethene also exhibited a trap temperature dependence similar to benzene, although not nearly as intense.

The partial pressure of methane did not change greatly (less than an order of magnitude) for various trapping conditions. However, the methane pattern repeatedly increased to the background level upon isolating the PPAS from the trap and diffusion pump. When the valve of the getter-ion pump was opened, the pressure of methane would fall to  $\sim 1.6 \times 10^{-11}$  Torr (air equivalent). This behavior indicated that there was a source of methane in the PPAS.

At this point, it is interesting to refer for a moment to another study which was conducted in this laboratory. This work involved determining the major residual-gas constituents in a liquid-nitrogen trapped mercury-diffusion-pumped glass and metal system. The analyzer used in this study was similar to that described above. Table II displays the residual gases following a bake of  $200^{\circ}\text{C}$ . The total-pressure measurement was made with a Redhead gauge.

Gas	Pressure (Torr-air equivalent units)
$\text{H}_2$	$1.7 \times 10^{-11}$
$\text{H}_2\text{O}$	$1.8 \times 10^{-11}$
CO	$1.5 \times 10^{-10}$
$\text{CO}_2$	$1.7 \times 10^{-11}$
Total	$2.0 \times 10^{-10}$

TABLE II. Major residual gases in  $\text{LN}_2$  trapped mercury-diffusion-pumped glass-metal uHV system.

Note that no detectable amount of methane was observed. This fact indicates that the analyzer itself is not generating significant amounts of methane.

The generation of methane from Bayard-Alpert type gauges with metal envelopes has been reported by Davis.<sup>5</sup> However, in the PPAS, the ionization gauges are mounted in glass envelopes. In order to explore further the possibility of the ion gauge being a methane source, a brief study was conducted to determine the effects of a hot tungsten filament and electron bombardment of metal-grid surfaces on the residual gas in the system.

The PPAS, the experimental trap, and the uHV line to the first diffusion pump were baked to  $400^{\circ}\text{C}$ , as outlined above. Following the bake and after cooling the trap to  $\text{LN}_2$  temperature, the operating parameters of the ionization gauges (shown in Fig. 1) were varied from a gauge-off condition to a modified outgas condition, i.e., near normal grid current with 350 V grid potential. It was observed that, following a brief transient condition, the amount of methane present was not affected greatly by the operation of the tungsten filament. However, increasing the grid potential from the normal level of 130 to 350 V did cause a significant increase in the methane level. Therefore, it was concluded that methane resided primarily in the ion gauge as an adsorbed species, rather than one which was generated by the combination of hydrogen and carbon at the hot filament surface. It would be expected that the amount of methane generation would vary from system to system, depending on the techniques used to obtain and measure evacuation. For example, no methane generation was observed for the glass-metal mercury-diffusion-pumped  $\text{LN}_2$  trapped system using a cold-cathode magnetron gauge discussed above. However, for the oil-diffusion-pumped/liquid nitrogen and zeolite-trapped glass-metal system using hot-filament ionization gauges, methane generation was observed, resulting from increased grid potential. It is likely in the latter case that adsorbed methane resides throughout the PPAS as a result of methane migration (both gaseous and surface) from the diffusion pump during the bakeout, i.e., before the zeolite trap was cooled to  $\text{LN}_2$  temperature.

The remaining gases in Table I do not appear to be greatly dependent upon the experimental trap temperature. However, there is a definite advantage indicated in the use of zeolite for reducing hydrocarbon contamination.

### III. Summary

A systematic study has been conducted to determine the effectiveness of an optically detectable zeolite-charged trap in reducing the gaseous contamination of uHV systems by an oil-diffusion pump using DC-705 pump-

ing fluid. Three trap-temperature conditions were studied. Two of these conditions were determined by submerging the experimental trap into a bath of either liquid nitrogen or dry ice and acetone. The third temperature was determined by ambient laboratory conditions.

The data collected by means of a sensitive partial-pressure analyzer indicated that a significantly lower level of contamination was achieved by cooling the zeolite trap to even  $-78^{\circ}\text{C}$  from room temperature.

Data were also taken of the trap operating without the chemical. Comparison of these sets of data indicates that a significant increase in trapping efficiency can be realized when zeolite is used. The greatest improvement over the nonchemical conditions was noted at the dry ice and acetone slurry temperature. A consideration of these results suggests that reasonably good trapping of uhv systems can be achieved by employing mechanically refrigerated zeolite traps above oil-diffusion pumps using DC-705.

## Physical-Adsorption Isotherm Based on a Triangular-Site Model\*

LYLE H. TAYLOR, WILLIAM W. LONGLEY, JR., AND PAUL J. BRYANT

Midwest Research Institute, Kansas City, Missouri

(Received 10 February 1965)

A multilayer physical-adsorption-isotherm theory is developed; it assumes that a gas atom cannot be physically adsorbed in an upper layer unless there is a triangular array of three adsorbed atoms in the layer below forming a site for adsorption. Neighbor interactions via Lennard-Jones intermolecular potentials are included in the calculation of the adsorption energy. The resultant isotherm is linear for low coverages, indicates a horizontal interaction correction to the Langmuir adsorption isotherm when there is only first-layer coverage, and may yield a series of steps for sufficiently low temperature. Numerical adsorption isotherms for He on glass at 4.28° and 77°K are presented. The former isotherm exhibits distinctive steps when each layer is condensed, whereas the latter isotherm is quite smooth.

### I. INTRODUCTION

MANY theories of physical adsorption have been proposed, and many modifications of these theories have been developed. This intensive effort is understandable since the phenomenon is extremely interesting and would seem to lend itself to precise experimental measurements and accurate theoretical descriptions. Experience has shown that physical adsorption is a function of many variables, e.g., molecular interactions, surface roughness, adsorption-site models, molecular vibrational states, etc. To avoid excessive cumbersomeness and difficulty, it is customary for any theory to incorporate only a few variables and to approximate or to ignore the remainder. This paper is no exception in that regard.

The derivation presented here has some different assumptions, but is analogous to the derivation, via the discipline of statistical mechanics, of the Brunauer-Emmett-Teller (BET) adsorption isotherm.<sup>1,2</sup> There are also similarities to Halsey's triangular-site model.<sup>3,4</sup> In the new theory, the mathematically flat surface with  $S_1$  fixed sites is borrowed from the BET theory. The variation of site energy with coverage of all

permitted layers is considered in greater detail than in either of the above-mentioned theories. This energy treatment is based on a Bragg-Williams model<sup>5</sup> for occupation assignment.

Section II details the numerous approximations used in this paper and describes the statistical-mechanical theory used to derive the physical-adsorption-isotherm equations based on a triangular-site model. Since treating molecular interactions causes the adsorption energy to vary as a function of coverage in all layers, an "effective" adsorption energy is defined in Sec. III. The adsorption isotherm equations are discussed in Sec. IV, and an iteration technique is presented. Two specific isotherms for helium on glass are calculated from this theory and discussed in Sec. V.

### II. GENERAL THEORY

The mathematically flat surface of the BET theory is used; however, the single-particle-single-site model of the BET theory is replaced by the more aesthetic triangular-site model of Halsey,<sup>4</sup> i.e., it is assumed that a particle cannot be adsorbed in an upper layer unless there is a triangular array of three adsorbed particles forming a site for adsorption. The BET and triangular-site models are compared diagrammatically in Fig. 1.

Let  $X_j$  represent the number of adsorbed particles in the  $j$ th layer. Then the total number of adsorbed

\* This work was supported by the National Aeronautics and Space Administration, Headquarters, Washington, D. C., under Contract NASr-63(06).

<sup>1</sup> W. C. Band, *Introduction to Quantum Statistics* (D. Van Nostrand Company, Inc., New York, 1955).

<sup>2</sup> S. Brunauer, P. H. Emmett, and E. Teller, *J. Am. Chem. Soc.* **60**, 309 (1938).

<sup>3</sup> G. D. Halsey, *Advan. Catalysis* **4**, 259 (1952).

<sup>4</sup> G. Halsey, *J. Chem. Phys.* **16**, 931 (1948).

<sup>5</sup> T. L. Hill, *Introduction to Statistical Thermodynamics* (Addison-Wesley Publishing Company, Inc., Cambridge, Massachusetts, 1960).

particles  $A$  is given by

$$A = \sum_{j=1}^J X_j,$$

where  $J$  is the total number of layers containing adsorbed particles. In addition, let each layer be mathematically flat and contain  $S_1$  fixed sites in the same configuration as those of the first layer but laterally displaced for close packing. Furthermore, assume that the probability of a given fixed site being occupied is  $\theta_j$ , where  $\theta_j = X_j/S_1$  is the fractional occupancy of the  $j$ th layer. This choice of occupation probability is consistent with the gas particles striking the adsorbing sites at random and being unable to migrate over the surface.

The next problem is to find the number of sites available for an adsorbed particle in the  $j$ th layer. The triangular-site model and the close-packed-array assumption make this quantity equal to the total number of possible sites, neglecting the site occupation rule, times the probability of simultaneous occupation of three adjacent fixed sites in the preceding layer, i.e.,

$$S_j = X_{j-1}\theta_{j-1}^2, \quad X_0 = S_1, \quad \theta_0 = 1. \quad (1)$$

Equation (1) replaces  $S_j = X_{j-1}$  in the BET theory. Now  $S_j$  need not be an integer. The generalized factorial, the gamma function, is used in the calculation of the total number  $W$  of independent ways to assign  $N$  indistinguishable particles to the over-all adsorption system (gas and adsorbate surface):

$$W = \prod_{j=1}^{\infty} \left( \frac{\omega_j^{n_j}}{n_j!} \right) \frac{\Gamma(S_j+1)}{\Gamma(X_j+1)\Gamma(S_j-X_j+1)}, \quad (2)$$

where  $\omega_i$  is the degeneracy weight of the  $i$ th energy level  $\epsilon_i$  of the gas and  $n_i$  is the number of gas particles in that energy level.

The statistical problem is to find the numbers  $X_j$  and  $n_j$  that give a maximum value to  $\sigma_s = \ln W$ , under the restrictions of a given total number of particles  $N$  and a given total energy  $E$ . The constraints on the system are given by

$$N = \sum_{j=1}^{\infty} (n_j + X_j), \quad E = \sum_{j=1}^{\infty} (n_j \epsilon_j + X_j W_j), \quad (3)$$

where  $W_j$  is the average energy of adsorption for each adsorbed particle in the  $j$ th layer.

Since  $N$  and  $E$  are constant and  $\sigma_s$  is a maximum, their variations must vanish. In performing the variational calculation, it is convenient to define the "effective" adsorption energy  $E_j$ , which obviously depends on the molecular interactions and interlayer-adsorption-energy variations, as follows:

$$E_j = W_j + \sum_{i=1}^J \theta_i \frac{dW_i}{d\theta_j}. \quad (4)$$

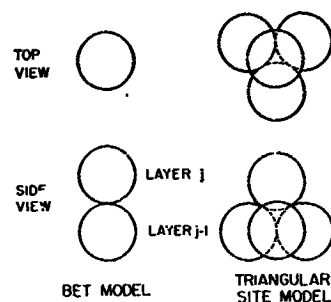


FIG. 1. Site models.

The variational calculation yields the following equations:

$$d\sigma_s/dn_i = \alpha + \beta \epsilon_i, \quad (5)$$

$$d\sigma_s/dX_j = \alpha - \beta E_j, \quad (6)$$

where  $\sigma_s = \sigma_g \sigma_a$ ,  $\sigma_a$  being that part of the product pertaining only to the adsorbed particles and  $\sigma_g$  that part pertaining only to the gas particles.

Equation (5) is the classical equation of an ideal gas of Boltzmann particles treated separately from the adsorbed layers. Assuming  $n_i$  to be very large leads to the identification of  $\alpha$  and  $\beta$  in terms of the chemical potential  $\mu$  and the absolute temperature  $T$  of the gas phase<sup>1</sup>:

$$\alpha = -\mu/k_0 T, \quad \beta = 1/k_0 T, \quad (7)$$

where  $k_0$  is Boltzmann's constant. The ideal gas law also follows:

$$\begin{aligned} pV &= N_g k_0 T, \\ N_g &= k_0^{-1} KV (MT)^{3/2} \exp(\mu/k_0 T), \\ K &= (2\pi k_0)^{3/2} k_0 h^{-3}, \end{aligned} \quad (8)$$

where  $V$  is the volume,  $p$  is the pressure,  $M$  is the mass of a gas particle, and  $h$  is Planck's constant. These results are derived from Boltzmann statistics which are valid<sup>1</sup> when  $\alpha$  exceeds 3.

It is now convenient to define a new parameter  $\gamma_j$ , such that

$$\gamma_j = \exp[-(\mu + E_j)/k_0 T] \quad (9)$$

and to evaluate this new parameter in terms of physically measurable parameters. From Eqs. (8) and (9) one obtains

$$\gamma_j = (KM^3 T^3 / p) \exp(-E_j/k_0 T). \quad (10)$$

Equation (6) can now be written as

$$d\sigma_a/d\theta_j = S_1 \ln \gamma_j. \quad (11)$$

The latter expression is the basic equation to solve in deriving the adsorption isotherm. By using Stirling's approximation for large arguments of the gamma functions in Eq. (2) and by differentiating the result, the

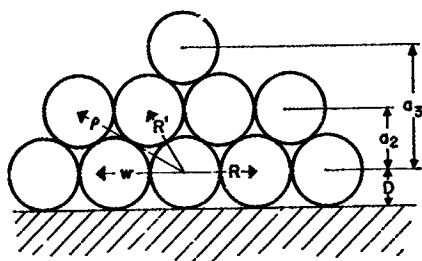


FIG. 2. Adsorption geometry.

left-hand side of Eq. (11) is evaluated. The final result is

$$\gamma_j = [(\theta_{j-1}^3 - \theta_j)/\theta_j][\theta_j^3/(\theta_j^3 - \theta_{j+1})]^{3\theta_j^2}. \quad (12)$$

The triangular-site physical-adsorption isotherm is obtained from the simultaneous solution of Eqs. (10) and (12).

### III. EFFECTIVE ADSORPTION ENERGIES

The energy of adsorption  $W_j$  is defined as the difference between the energy of a free particle at rest and the average energy of an adsorbed particle in the  $j$ th layer. Equation (4) shows that the effective adsorption energy  $E_j$  is completely determined when all the  $W_j$ 's are known.

It is assumed that the intermolecular potential  $\phi$  between two adsorbed molecules can be closely approximated by the Lennard-Jones ( $n$ - $m$ ) potential for spherically symmetric molecules:

$$\phi(r) = \frac{\epsilon}{m-n} \left( \frac{m}{n} \right)^{1/(m-n)} \left[ \left( \frac{\sigma}{r} \right)^m - \left( \frac{\sigma}{r} \right)^n \right], \quad m > n, \quad (13)$$

where  $r$  is the distance between the molecules,  $\sigma$  is the distance of closest approach of two molecules which collide with zero initial relative kinetic energy, and  $\epsilon$  is the maximum energy of attraction of the two molecules when the repulsive term is also considered.<sup>6</sup> If  $R$  represents the equilibrium distance between the adsorbed molecules, it is necessary that  $\phi$  be a minimum at  $R$ , i.e.,

$$R = (m/n)^{1/(m-n)} \sigma. \quad (14)$$

Since  $\phi$  is an energy per pair of gas molecules, and since  $W_j$  is an energy per gas molecule, each pair that includes one specific molecule will contribute  $\frac{1}{2}\phi(r)$  to  $W_j$  for that molecule.

The intermolecular potential  $\phi_s$  between an adsorbed molecule and an adsorbent molecule is approximated by another Lennard-Jones potential:

$$\phi_s(r) = \frac{\epsilon_s}{k-l} \left( \frac{k}{l} \right)^{1/(k-l)} \left[ \left( \frac{\sigma_s}{r} \right)^k - \left( \frac{\sigma_s}{r} \right)^l \right], \quad k > l. \quad (15)$$

Since the change of potential at an adsorbent molecule

is not considered, the entire value of  $\phi_s$  will be assigned to  $W_j$  for the adsorbed molecule.

The term "physical adsorption" can now be explicitly defined as that adsorption for which  $k > l > 3$  and  $m > n > 3$ . In other words, attractive forces arising from ionic charges and permanent dipoles are excluded from consideration.

Integration of the intermolecular potential of gas and adsorbent molecules over the volume occupied by the solid leads to an evaluation of the adsorbent contribution  $W_{s1}$  to the adsorption energy  $W_j$ . The integration implies that the intermolecular potentials are additive. This latter assumption is probably more serious than any made thus far,<sup>7</sup> but it is necessary for any simple and usable theory.

With the surface located a distance  $D$  below the centers of the adsorbed molecules in the first layer (see Fig. 2),  $W_{s1}$  is given by

$$W_{s1} = W_s = 2\pi\epsilon_s N_0 D^3 \left( \frac{k}{l-2} \right)^{k/(k-l)} \left( \frac{k-2}{l} \right)^{l/(k-l)} \frac{1}{(k-3)(l-3)}, \quad (16)$$

where

$$D = [(l-2)/(k-2)]^{1/(k-l)} \sigma_s \quad (17)$$

and  $N_0$  is the number of adsorbent molecules per unit volume. The energy of interaction  $W_{s1}$  was chosen to be a maximum for the particular potential used, thus explaining why  $D$  is less than  $\sigma_s$ .

The adsorbate layers are assumed to be equally spaced at intervals  $a$  from each other. Thus, the distance between the first layer and the  $j$ th layer (as indicated in Fig. 2) is  $a_j$ , where

$$a_j = (j-1)a = Dd_j. \quad (18)$$

The adsorbent contribution to  $W_j$  is given by

$$W_{sj} = \frac{W_s}{k-l} \left[ \frac{k-3}{(1+d_j)^{l-3}} - \frac{l-3}{(1+d_j)^{k-3}} \right]. \quad (19)$$

An adsorbed molecule interacts with the adsorbent and all other adsorbed molecules. The interactions between the molecules of the  $i$ th layer and a specific molecule in the  $j$ th layer are labeled  $W_{ij}$ . The adsorption energy can be determined by summing  $W_{sj}$ , which has already been evaluated, and all  $W_{ij}$ . The  $W_{ij}$  are individually evaluated below by treating the nearest-neighbor interactions exactly and approximating the remaining interactions.

The evaluation of  $W_{j+2,j}$  is interesting since the molecules in the  $(j+2)$ th layer may be positioned in two possible ways. If these molecules lie above those in the  $j$ th layer, the hexagonal close-packed crystalline structure results. Otherwise, the face-centered-cubic structure is obtained. But there is virtually no differ-

<sup>6</sup> J. O. Hirschfelder, C. F. Curtiss, and R. B. Bird, *Molecular Theory of Gases and Liquids* (John Wiley & Sons, Inc., New York, 1954).

<sup>7</sup> J. R. Sams, G. Constabaris, and G. D. Halsey, Jr., *J. Chem. Phys.* **36**, 1334 (1962).

ence in energies between these two crystalline structures. Therefore, the interaction energy is evaluated by representing the  $(j+2)$ th layer as a plane and integrating over it. The result is

$$W_{lj} = \theta_l z(|a_i - a_j|), \quad (20)$$

where

$$z(r) = \frac{2\pi\epsilon r^2}{\sqrt{3}(m-n)R^2} \left(\frac{m}{n}\right)^{1/(m-n)} \left[ \frac{1}{n-2} \left(\frac{\sigma}{r}\right)^n - \frac{1}{m-2} \left(\frac{\sigma}{r}\right)^m \right]. \quad (21)$$

The subscript  $l$  is used in Eq. (20) since it can be used for any layer that does not contain a nearest neighbor to the particle in the  $j$ th layer. Equation (20) will be used for all  $l$  except  $j-1, j$ , and  $j+1$ .

The evaluation of the  $W_{j-1,j}$  interaction energy is straightforward and is done by summing over the three nearest neighbors at distance  $R'$  (see Fig. 2) and by integrating over the remainder of the  $(j-1)$ th layer. The result is

$$W_{j-1,j} = [\theta_{j-1} z(\rho) - \frac{3}{2} \phi(R')] f_j', \quad (22)$$

where  $f_j' = 1 - \delta_j^1$  relates  $f_j'$  to the Kronecker delta and  $\rho$  is, for the moment, an arbitrary distance used in both the  $(j-1)$ th and  $(j+1)$ th layers as illustrated in Fig. 2.

The  $W_{j-1,j}$  interaction energy is treated in a like manner. The integrated term is exactly analogous to that in Eq. (22), but the factor  $3/2$  appearing in the other term must be replaced by a probability function, because the three nearest neighbors are no longer involved in forming the triangular adsorption site and, hence, cannot be assured of existence. This probability function  $P_j$  is evaluated as

$$P_j = (\theta_{j+1}/3\theta_j^3) P_{j-1}^2, \quad P_0 = 3\theta_1. \quad (23)$$

Therefore, the contribution of the  $(j+1)$ th layer to  $W_j$  is

$$W_{j+1,j} = \theta_{j+1} z(\rho) - \frac{1}{2} P_j \phi(R'). \quad (24)$$

Likewise, the  $W_{jj}$  interaction energy is evaluated to be

$$W_{jj} = \theta_j z(w) + P_{j-1} \epsilon, \quad (25)$$

where  $w$  is another arbitrary distance (see Fig. 2).

The values of  $w$  and  $\rho$  must be ascertained in a systematic manner. The chosen method of determining  $w$  is to require the integration result (for  $\theta_j = 1$ ) at  $w$  to equal the correct result obtained by actually summing over the six next-nearest neighbors lying within the  $j$ th layer. Thus,  $w$  is determined to be

$$w = [2\pi/(n-2)\sqrt{3}]^{1/(n-2)} \sqrt{3}R. \quad (26)$$

Using a comparable argument for  $\rho$ , we obtain

$$\rho = [4\pi(4R^2 + 3a^2)/\sqrt{3}9(n-2)R^2]^{1/(n-2)} (\frac{1}{3}R^2 + a^2)^{\frac{1}{2}}. \quad (27)$$

The adsorption energy is determined by adding the above interaction energies to give

$$W_j = W_{sj} - \frac{1}{2}(3f_j' + P_j)\phi(R') + P_{j-1}\epsilon + \theta_j z(w) + (f_j'\theta_{j-1} + \theta_{j+1})z(\rho) + \sum_{i=1}^{j-2} \theta_i z(a_j - a_i) + \sum_{i=j+2}^J \theta_i z(a_i - a_j). \quad (28)$$

Equation (4) can now be applied to this equation to yield the effective adsorption energy

$$E_j = W_{sj} + 2P_{j-1}\epsilon - \frac{1}{2}(3 + P_{j-1}\theta_{j-1}/\theta_j) f_j' \phi(R') - \sum_{i=j+1}^J \frac{2^{i-j-1} \theta_i [P_{i-1}\epsilon - P_i \phi(R')]}{\theta_j} + 2\theta_j z(w) + 2(f_j'\theta_{j-1} + \theta_{j+1})z(\rho) + 2 \sum_{i=1}^{j-2} \theta_i z(a_j - a_i) + 2 \sum_{i=j+2}^J \theta_i z(a_i - a_j). \quad (29)$$

#### IV. ADSORPTION ISOTHERM

The triangular-site physical-adsorption equations cannot be solved exactly but must be solved iteratively. The  $k$ th iterative solution is obtained by rearranging Eq. (12) to give

$$\theta_j^{(k)} = \theta_{j-1}^{(k)} [1 + \gamma_j (1 - \theta_{j+1}^{(k-1)} \theta_j^{(k-1)})^{-1}]^{-1}, \quad (30)$$

where the right-hand side is evaluated by using the  $k$ th iterative values for all  $\theta_i$ ,  $i < j$  and the  $(k-1)$ th iteration values for all  $\theta_i$ ,  $i \geq j$ . The exact theory is obtained when the iteration converges.

Starting values for the exact theory can be obtained either from intelligent guesses or from the approximate theory. The approximate theory, which sets  $\theta_i = 0$  for  $i > j$  and neglects the  $\theta_j$  dependence of  $\gamma_j$ , has many interesting properties. For example, when

$$p \ll KM^{\frac{1}{2}} T^{\frac{1}{2}} \exp(-W_s/k_0 T), \quad (31)$$

it is shown that the percent coverage is directly proportional to the pressure. This linear dependence has been verified for Kr, Ar, and Ne on P33 carbon black.<sup>8</sup> In the range where Eq. (31) is invalid but only monomolecular adsorption is occurring, the approximate theory reduces to the conventional Langmuir adsorption isotherm for a single adsorbed layer.

The exact theory is based on a solid-state approach to the adsorbed layers and must become invalid when the temperature is above the melting point of the adsorbate or if the resultant crystalline structure is neither face-centered cubic nor hexagonal close packed. (Evidence<sup>9</sup> has been presented suggesting that helium

<sup>8</sup> G. Constabaris, J. H. Singleton, and G. D. Halsey, Jr., J. Phys. Chem. **63**, 1350 (1959).

<sup>9</sup> J. G. Aston, S. V. R. Mastrangelo, and R. J. Tykodi, J. Chem. Phys. **23**, 1633 (1955).

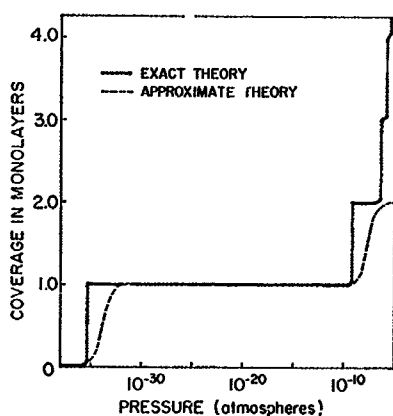


FIG. 3. Adsorption isotherm for helium on porous glass at 4.28°K.

adsorbs onto titanium dioxide in a solid-state lattice.) One of the more interesting features of the exact theory is that  $E_j$  passes through a maximum and then decreases as the pressure is increased. However, a close examination of Eq. (29) shows that this maximum should *almost* coincide with the event of  $\theta_{j+1} = \theta_j^2$ , and from Eq. (30) this equality cancels any variation of  $\gamma_j$ . Thus far, numerical calculations (see Sec. V) have shown the cancellations to be the case.

## V. NUMERICAL RESULTS

In order to make numerical predictions, certain parameters needed to evaluate the  $E_j$ 's are based on measurements by different methods. Halsey,<sup>10</sup> by fitting adsorption data to a 3- $\infty$  potential, has measured the values of  $D$  and  $W_s$  for six different adsorbates on porous glass and eight adsorbates on P33 graphitized carbon black. Gas-gas force constants,  $\sigma$  and  $\epsilon$ , are given in Hirschfelder, Curtiss, and Bird.<sup>6</sup> Based on the assumption of ideal hexagonal close-packed or face-centered cubic structure ( $R' = R$ ), the values of  $a$ ,  $w$ , and  $\rho$  can be calculated from the gas-gas  $R$  value.

The approximate and exact theories were both

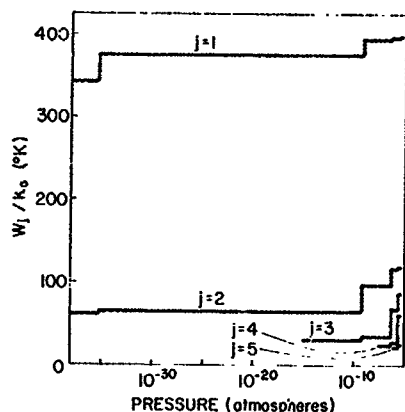


FIG. 4. Energies of adsorption for helium on porous glass at 4.28°K.

<sup>10</sup> G. D. Halsey, Jr., Trans. Natl. Vac. Symp. 1961, 119 (1962).

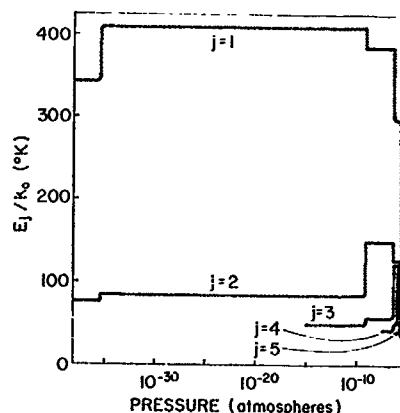


FIG. 5. Effective adsorption energy for helium on porous glass at 4.28°K.

applied to calculate triangular-site adsorption isotherms for helium on porous glass at temperatures of 4.28° and 77°K. The former isotherm is plotted in Fig. 3 where "monolayer coverage"  $\theta$  is defined as the ratio of the total number of adsorbed molecules to the number of sites present on the adsorbent, i.e.,  $A/S_1$ . The approximate theory appears to be fairly good for  $\theta < 2$ , but fails badly at higher coverages. However, the most striking features of Fig. 3 are the very abrupt steps exhibited by the exact theory. This apparent condensation is physically attributable to the intralayer molecular interactions. If the classical second virial coefficient value<sup>6</sup> of  $\epsilon/k_B$ , 6.03°K, were used, the pressures which permit second- and higher-level coverages to become appreciable would be raised by a factor of  $\sim 100$ . Thus, the theory indicates a strong dependence on the value of  $\epsilon$ .

The adsorption energies and effective adsorption energies are plotted in Figs. 4 and 5, respectively. Note that the adsorption energies are monotonically increasing, whereas the effective adsorption energies for the first three layers exhibit maxima. However, no physical effect of the maxima is predicted since, whenever  $E_j$  decreases, the multiplicative factor of  $\gamma_j$  in Eq. (30) is always zero due to filling of the  $(j+1)$ th layer.

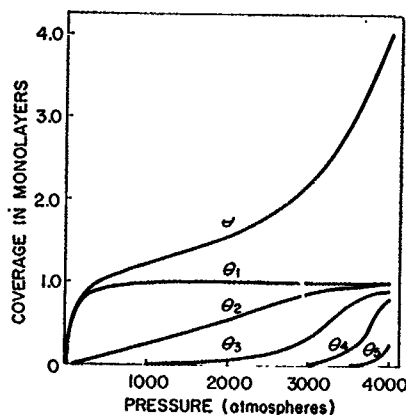


FIG. 6. Adsorption isotherm for helium on porous glass at 77°K.

The triangular-site adsorption isotherm for helium on glass at 77°K is plotted in Fig. 6. Notice the smooth curves and partially filled layers as contrasted with the single-layer condensation steps of Fig. 3. As expected, the adsorption energies shown in Fig. 7 are smoothly and monotonically increasing. Contrary to the results at 4.28°K, the effective adsorption energies plotted in Fig. 8 exhibit maxima which do not coincide exactly with the vanishing of the  $\gamma_j$  multiplier in Eq. (30). The physical effect of this noncoincidence is shown in Fig. 6 by the gradual approach of  $\theta_1$  and  $\theta_2$  to 1. Another interesting result, excluding the first two layers, is indicated in Fig. 8 by the extremely high effective adsorption energy for the top layer at very low coverages.

## VI. CONCLUSIONS

The *numerical* isotherms given in the previous section cannot be interpreted as bona fide predictions, e.g., in Fig. 3 the saturation pressure of helium is around  $10^{-6}$  atm, whereas the actual saturation pressure is, of course, 1 atm. The error caused by not using weakly degenerate quantum statistics for the gas affects the higher-pressure data of Fig. 6 to some extent. The improper saturation pressure is probably related to the use of the Bragg-Williams model. But more sophisticated models<sup>11</sup> also have inherent difficulties. However,

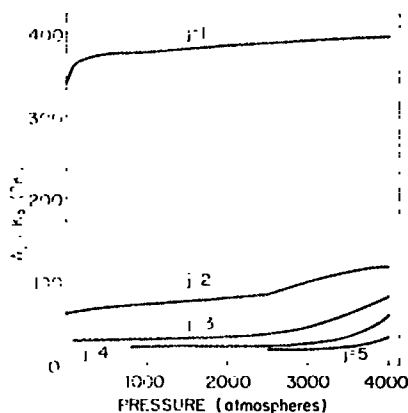


FIG. 7. Energies of adsorption for helium on porous glass at 77°K.

<sup>11</sup> P. C. Hemmer, *J. Math. Phys.* **5**, 75 (1964).

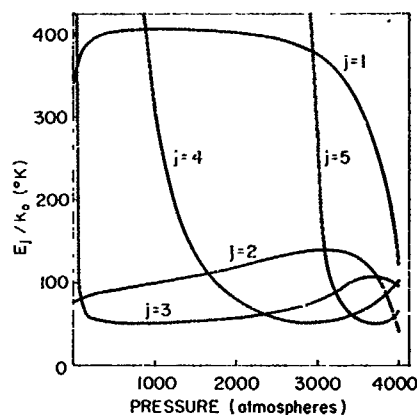


FIG. 8. Effective adsorption energy for helium on porous glass at 77°K.

the numerical isotherms are good examples of adsorption isotherms which may be obtained from the theory. For example, single-layer condensation steps similar to those in Fig. 3 have been observed for krypton on P33 carbon black by Singleton and Halsey,<sup>12</sup> who attribute them to the flatness of the surface—a basic assumption of this paper. On the other hand, the higher-temperature adsorption isotherm of Fig. 6 has the general appearance of many published isotherms.

The main difficulty in using the triangular-site adsorption isotherm is in obtaining values of  $D$ ,  $W_s$ ,  $a$ ,  $\sigma$ , and  $\epsilon$ . However, Halsey<sup>10</sup> has measured  $D$  and  $W_s$  for two adsorbents and 11 adsorbates. The interlayer spacing  $a$  is not accurately known. The well-published gas-gas values of  $\sigma$  and  $\epsilon$  can be used, although Steele<sup>13</sup> found that for helium  $R$  increased 30% when the helium was adsorbed. Moreover, for argon on P33 carbon black, Sams *et al.*,<sup>7</sup> observed that the Lennard-Jones (6-12) force constants were changed by about 20% from the gas-gas values. A combination of the proper set of  $W_s$ ,  $\epsilon$ ,  $R$ , and  $a$  values may reduce the present need for a saturation-pressure correction. Indeed, the theory does suggest that data for the difficult systems of helium and any solid at very low temperatures might be fitted by proper choice of parameters.

<sup>12</sup> J. H. Singleton and G. D. Halsey, Jr., *Can. J. Chem.* **33**, 184 (1955).

<sup>13</sup> W. Steele, Jr., *J. Chem. Phys.* **25**, 819 (1956).